

ESA Climate Change Initiative (CCI+) Essential Climate Variable (ECV) Antarctica_Ice_Sheet_cci+ (AIS_cci+)

Algorithm Theoretical Basis Document (ATBD) for CCI+ Phase 1

Prime & Science Lead: Andrew Shepherd
University of Leeds, Leeds, United Kingdom
a.shepherd@leeds.ac.uk

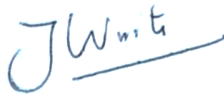


Technical Officer: Marcus Engdahl
ESA ESRIN, Frascati, Italy
Marcus.Engdahl@esa.int

Consortium:
DTU Microwaves and Remote Sensing Group (DTU-N)
DTU Geodynamics Group (DTU-S)
ENVironmental Earth Observation GmbH (ENVEO)
Deutsches Zentrum für Luft- und Raumfahrt (DLR) Remote Sensing Technology
Institute (IMF)
Science [&] Technology AS (ST)
Technische Universität Dresden (TUDr)
University College London (UCL/MSSL)
University of Leeds, School of Earth and Environment (UL)





Signatures page

Prepared by	Jan Wuite Lead Author, ENVEO		Date: 6 Mar 2020
Issued by	Daniele Fantin, Project Manager, S[&]T		Date: 6 Mar 2020
Checked by	Andrew Shepherd Science Leader, UL		Date: 9 Mar 2020
Approved by	Marcus Engdahl ESA Technical Officer		Date:

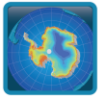
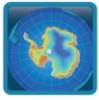


Table of Contents

Change Log	5
Acronyms and Abbreviations	6
1 Introduction	7
1.1 Purpose and Scope	7
1.2 Document Structure	7
1.3 Applicable and Reference Documents.....	7
2 Surface Elevation Change	8
2.1 Introduction	8
2.2 Review of scientific background.....	8
2.3 Algorithms.....	10
2.3.1 Plane fit	10
2.3.2 Cross-calibration	12
2.4 Input data and algorithm output	13
2.5 Accuracy and performance	14
2.6 Capabilities and known limitations	16
2.7 References	16
3 Ice Velocity	19
3.1 Introduction	19
3.2 Review of scientific background.....	20
3.3 Algorithms.....	20
3.3.1 Generation of Groundline Mask	21
3.3.2 Retrieve Geolocation Grid.....	22
3.3.3 Compute Local Incidence Angle.....	22
3.3.4 Simulation of differential Tide	22
3.3.5 Simulation of differential Surface pressure	23
3.3.6 Correction of atmospheric and tidal induced iv variations	24
3.4 Input data and algorithm output	24
3.4.1 Uncorrected iv-map in SAR geometry at burst level	24
3.4.2 Tide Model	24
3.4.3 Mask of Grounded Ice.....	24
3.4.4 Reanalysis Data of Surface Pressure	25
3.4.5 Digital Elevation Model.....	25
3.5 Accuracy and performance	25
3.6 Capabilities and known limitations	26
3.7 References	27
4 Appendix 1 – Round Robin Ice Velocity on Ice Shelves	28
4.1 Introduction	28
4.2 Test Area & Reference Velocity.....	28
4.3 Round Robin Package & Steps.....	29
4.4 Results.....	30
4.4.1 Tidal Correction Methods.....	30
4.4.2 Participant Intercomparison.....	31
4.4.3 Reference Intercomparison.....	34



4.4.4 Tide Model Intercomparison.....37

4.4.5 Surface Pressure Reanalysis Dataset Comparison39

4.5 Summary & Conclusions..... 40

4.6 Feedback Forms..... 41

4.6.1 Enveo.....41

4.6.2 DLR.....44

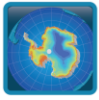
4.6.3 DTU.....45

4.7 References 47



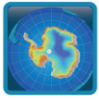
Change Log

Issue	Author	Affected Section	Change	Status
1.0	ENVEO	All	Document Creation	



Acronyms and Abbreviations

Acronyms	Explanation
AIS	Antarctic Ice Sheet
ATBD	Algorithm Theoretical Basis Document
CCI	Climate Change Initiative
DEM	Digital Elevation Model
DInSAR	Differential SAR Interferometry
DLR	Deutsches Zentrum für Luft- und Raumfahrt
DTU	Danmarks Tekniske Universitet
ENVEO	Environmental Earth Observation
ERS	European Remote Sensing satellite
GG	Geolocation Grid
GLL	Grounding Line Location
GMB	Gravimetric Mass Balance
GPS	Global Positioning System
IBE	Inverted Barometric Effec
InSAR	Interferometric synthetic-aperture radar
IV	Ice Velocity
IVonIS	Ice Velocity on Ice Shelves
IW	Interferometric Wideswath
LRM	Low Resolution Mode
MIDAS	Impact of Melt on Ice Shelf Dynamics And Stability
REAPER	Reprocessing of Altimeter Products for ERS
REMA	Reference Elevation Model of Antarctica
RMSE	Root-Mean-Square Error
RR	Round Robin
S&T	Science and Technology AS
SAR	Synthetic Aperture Radar
SARIn	Synthetic Aperture Radar Interferometry
SEC	Surface Elevation Change
SLC	Single Look Complex
SNR	Signal to Noise Ratio
SPD	Surface Pressure Difference
TCOG	Threshold offset Centre Of Gravity
TUDr	Technische Universität Dresden
UCL	University College London
UL	University of Leeds



1 Introduction

1.1 Purpose and Scope

This document contains the Algorithm Theoretical Basis for the Antarctic Ice Sheet cci (AIS_cci) project for CCI+ Phase 1, in accordance to contract and SoW [AD1 and AD2]. The ATBD describes the scientific background and principle of the algorithms, their expected or known accuracy and performance, input and output data, as well as capabilities and limitations.

The ATBD for the Antarctic Ice Sheet cci project [RD1] is used as a basis for this work. It describes the algorithms used to generate the ECV parameters 'Surface Elevation Change (SEC)', 'Ice Velocity (IV)', 'Grounding Line Location (GLL)' and 'Gravimetric Mass Balance (GMB)'. The current document is a supplement to this, and the aim is to review and provide an update regarding improvements to existing algorithms for SEC and IV, proposed for CCI+.

1.2 Document Structure

This document is structured into an introductory chapter followed by 2 chapters focussed on the retrieval algorithms for the CCI+ parameters:

- Surface Elevation Change (SEC)
- Ice Velocity (IV)

In Appendix 1 the results for the Round Robin on IV on Ice Shelves (IVonIS) are presented.

1.3 Applicable and Reference Documents

Table 1.1: List of Applicable Documents

No	Doc. Id	Doc. Title	Date	Issue/ Revision/ Version
AD1	ESA/Contract No. 4000126813/19/I-NB, and its Appendix 2	CCI+ PHASE 1 - NEW R&D ON CCI ECVS, for Antarctica_Ice Sheet_cci	2019.09.30	
AD2	ESA-CCI-EOPS-PRGM-SOW-18-0118 Appendix 2 to contract.	Climate Change Initiative Extension (CCI+) Phase 1, New R&D on CCI ECVs Statement of Work	2018.05.31	Issue 1 Revision 6

Table 1.2: List of Reference Documents

No	Doc. Id	Doc. Title	Date	Issue/ Revision/ Version
RD1	ST-UL-ESA-AISCCI-ATBD-001_v1.0	ATBD for the Antarctic Ice Sheet CCI project of ESA's Climate Change Initiative	2017.11.01	3.0

Note: If not provided, the reference applies to the latest released Issue/Revision/Version

2 Surface Elevation Change

2.1 Introduction

Satellite altimetry provides estimates of ice sheet elevation changes through repeated measurements of ice sheet surface elevations. The technique has been employed to study both Greenland (Johanessen et al., 2005; Zwally et al., 2005; Zwally et al., 2011; Sørensen et al., 2011; Khvorostovsky 2012) and Antarctica (Wingham et al., 1998; Davis et al., 2005; Zwally et al., 2005), and has the distinct advantage of being able to resolve the detailed pattern of mass imbalance, with frequent (up to monthly) temporal sampling. Radar altimetry, in particular, provides the longest continuous observational record of all geodetic techniques (Wingham et al., 2009).

Altimeters using microwave frequencies are commonly referred to as radar altimetry. At these wavelengths the signal can penetrate cloud cover, making the measurements possible in all weather conditions. In addition, the use of microwaves enables measurements to be made independently from sunlight conditions. The satellites with altimeters on board are placed in repeat orbits (covering a region of up to 1 km on either side of a nominal ground track) enabling systematic monitoring of the Earth. Furthermore, satellite altimetry radars have been in continuous operation since 1991 and new missions are scheduled for the next decade. There is therefore the availability of long time series and as a consequence the possibility to monitor seasonal to inter-annual variations during the lifetime of these satellites.

The specific objectives of this chapter are:

- to provide the theoretical basis of the algorithms that will be used to generate elevation changes maps from radar altimeter data;
- to assess the accuracy of these products; and
- to evaluate the range of applicability and the limitations of the derived data.

2.2 Review of scientific background

Radar altimeters provide a measure of the time, t_d , of a radio signal to travel from the emitting instrument, reach a target surface, and return/scatter back. The distance from the reflecting target to the radar is given by (Elachi, 1988):

$$r = \frac{ct_d}{2} \quad \text{Equation 2.1}$$

where c is the speed of light. The accuracy with which the distance is measured is given by

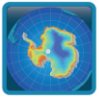
$$\Delta r = \frac{c}{2B} \quad \text{Equation 2.2}$$

where B specifies the signal bandwidth. The operating principle of an altimeter is shown in Figure 2.1 (a). Surface elevation h is calculated as the difference between the satellite altitude, a , and the measured range, r :

$$h = a - r \quad \text{Equation 2.3}$$

h is relative to the reference ellipsoid used for determining satellite altitude (see Figure 2.1 a). In addition to measuring range, the altimeter records a sample of the pulse echo return and estimates other parameters, including the magnitude of the return.

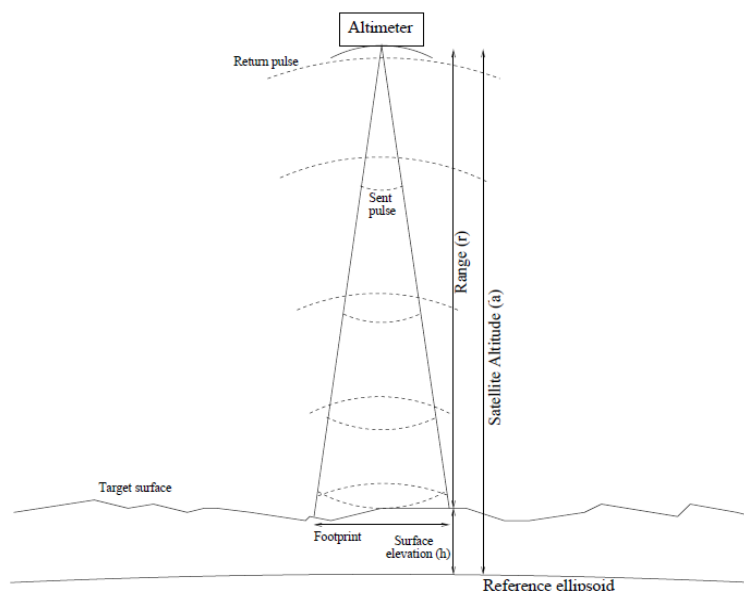
The side view representation in Figure 2.1 (b) shows the propagation of a single pulse along the beam of the antenna towards a horizontal and planar surface. The curved lines represent the pulse propagating and the temporal width between the curves is constant and equal to ϕ , the duration of the pulse length. A different visualization of the propagation (looking down on the scattering surface from the instrument position) is provided in Figure 2.1 b) (plane view). When the spherical wavefront first hits the surface at the instant time t_0 , the footprint is a point. The area illuminated by the pulse increases to a circular area until the trailing edge of the wavefront reaches the surface, at the instant time t_1 . The pulse-limited



footprint is the maximum circular area defined as the radius of the leading edge of the pulse when the trailing edge of the pulse first hits the surface. As the pulse propagates, the circle transforms into rings of equal area (Fu and Cazenave, 2001). The figure shows also a typical return waveform. The power received begins to increase from the time when the wavefront hits the surface, t_0 , and continues to increase for the duration of the pulse. The waveform presents a linear leading edge corresponding to this initial interaction. At the times greater than the pulse duration, the area intercepted by the pulse remains constant with time. But, instead of remaining constant, the power of the reflected pulse actually decreases gradually with time according to the illumination pattern of the antenna. The mid-point of the leading edge corresponds to the range to the mean surface within the pulse-limited footprint.

Information about surface roughness is obtained from waveform analysis. When a pulse scatters from a surface, the returned echo has a shape reflecting the (statistical) properties of the surface. In the case of the ocean, where the surface is homogeneous, the height statistics are the main factors in determining the pulse shape. In the case of terrain, the surface composition varies across the antenna footprint and its statistical properties need to be taken into account. For a perfectly smooth surface, the echo is a mirror image of the incident pulse. If the surface has some roughness, some return occurs in the backscatter direction at slight off-vertical angles as the pulse footprint spreads on the surface. This results in a slight spread in time of the echo. If the surface is very rough, some of the energy is scattered when the radio pulse intercepts the peaks of the surface and more energy is scattered as the pulse intercepts areas at various heights of the surface. This leads to a larger multi-path spread of energy which results in noticeable rise in the echo leading edge. The rise is used to measure the surface roughness.

The propagation of the pulse with time, as described above, assumes the forming of the returns is by scattering from the surface only. However, it has been shown that ice sheet returns consist of a combination of surface and sub-surface volume scattering due to penetration of part of the radar signal through the snow surface (Ridley and Partington, 1988). Volume scattering mainly results from the presence of in-homogeneities in the host medium, like ice grains, air bubbles, and ice inclusions, whose size, shape, density, dielectric constant, and orientation affect the scattering. They cause a redistribution of the energy of the transmitted wave into other directions and results in a loss in the transmitted wave (Ulaby et al., 1982). Signal penetration is largest in the dry snow zone of the ice sheets and can exceed 5 m (Davis and Poznyak, 1993; Legresy and Remy, 1998).



(a)

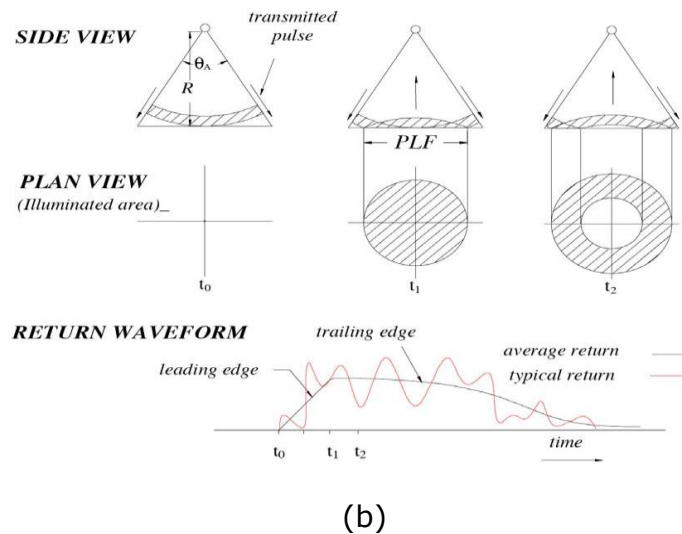


Figure 2.1: (a) Altimeter measurement principle; (b): The interaction of a radar altimeter pulse with a horizontal and planar surface, from its initial intersection (t_0), through the intersection of the descending edge of the wavefront with the surface (t_1), to the stage where the pulse begins to be attenuated by the antenna beam (t_2). The return is from surface only (Ridley and Partington, 1988).

Over ice sheet surfaces, the on-board tracker is generally unable to keep the leading edge of the waveform centred on the tracking point of the waveform window, and waveform retracking is to be applied to determine this offset. Several methods were developed for retracking ice sheet radar altimeter data (e.g. Bamber, 1994; Davis, 1997; Zwally and Brenner, 2001; Legresy et al., 2005). Retracking algorithms are based on defining the point where the waveform exceeds a certain percentage of the maximum power (threshold retrackers) or on functional fits to model waveform shape. All retrackers have their advantages and disadvantages, and selection of the retracker will affect taking of topography and volume scattering into account. Functional-fit retrackers more accurately produce individual elevation estimates, while threshold retrackers could be preferred for elevation change studies because they give more repeatable elevations.

2.3 Algorithms

The AIS CCI project performed extensive evaluation of several methods for deriving surface elevation change timeseries. These are documented in the AIS CCI ATBD (RD1). Only the algorithms that were used and will continue to be used in the CCI+ project, are described below.

2.3.1 Plane fit

In an ideal case, ground-tracks or spot tracks for altimeter satellites in repeat-track orbits (like Envisat 2003-10, and ICESat) would repeat exactly so that elevations along the track at one time could be directly compared to elevations along the same track obtained at a different time. However, differences in the altimeter pointing angle and orbital perturbations will cause across-track differences, which should therefore be compensated for within the repeat track analysis. The unmeasured topography between near repeat-tracks also needs to be considered when comparing elevations from different tracks. Due to these considerations, instead of differencing individual tracks, the plane-fit method is used to model the surface change in individual geographical grid cells, using data from many tracks, both ascending and descending, simultaneously.

Recently, it has been found advisable for the algorithm to take more factors into account, as there may exist a correlation between backscatter power and surface elevation. Further, there may exist anisotropy in the measurements, i.e. a bias between measurements made during ascending passes and those made during descending passes. Terms to estimate the latter can be included in the surface model (McMillan et al. 2014). Elevation effects due to backscatter are removed by two extra steps that follow the surface

modelling. Once the surface modelling step calculates the surface components of the modelled elevations, they are removed from the measured elevations to leave the temporal change and residual elements. A second modelling step determines the anisotropy of the backscatter component of the elevations, allowing removal of that component too. Finally, a linear fit correlates backscatter with elevation and is used to calculate a correction value applicable to a given time. The linear fit may only use data within a certain time period.

The plane fit algorithm (McMillan, *et al.*, 2014) is an adaption of the along track method which can be applied to satellites which operate in both short 27-35 day orbit repeat periods (such as the main operational periods of Envisat, ERS-1,2 and Sentinel-3A,B) and long 369 day repeat periods where measurements do not exactly repeat within monthly time scales such as CryoSat-2. This method can also be used with orbit locations relocated to the true echo location such as with CryoSat SARin mode. Figure 2.2 shows how the layout of data points in an example grid cell varies with sensor and orbit pattern and how the measurements are gridded using along track and plane fit methods.

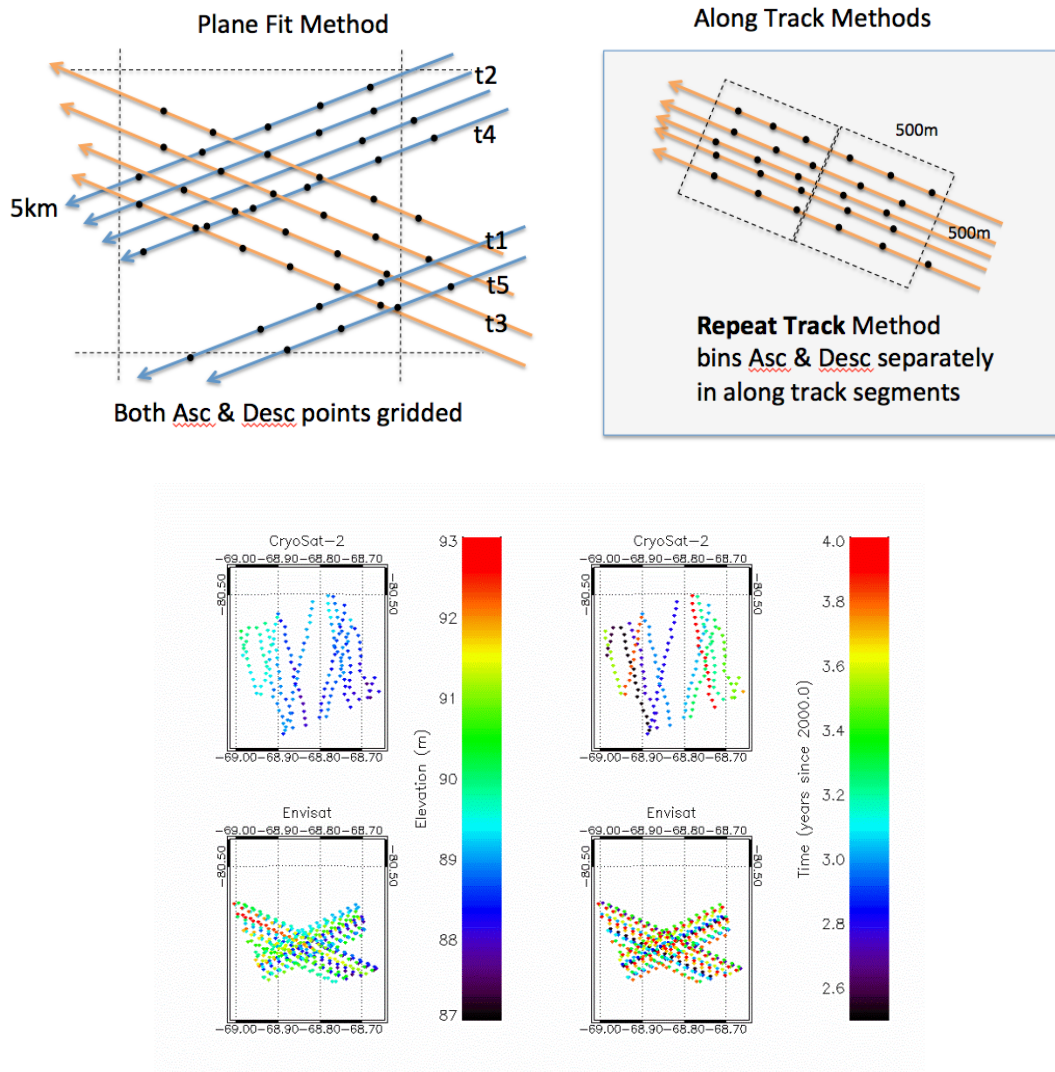


Figure 2.2: Example 5km by 5km grid cell on Filchner Ronne Ice Shelf, data points taken within an 18 month period. Locations slope-corrected. Measured elevations on left, timestamps on right.



The plane fit method grids both ascending and descending measurements in a regular polar stereographic grid instead of gridding separately along track. It derives a SEC estimate at the centre of each grid cell by applying a surface model to the measurements within that cell and has been shown in the CCI round robin experiments to perform as well or better than other along track methods for all missions (except Envisat's drifting phase from Oct 2010- Apr 2012, where special techniques are required for all methods) and hence was the primary along track method chosen for the Antarctic CCI. Another advantage of the plane fit method is that SEC results are produced on the same grid as the SEC output product and hence do not require re-gridding which can introduce an additional error and reduce accuracy.

Elevation changes are computed for each mission, for each geographical grid cell. Data falling within grid cells are only used to compute elevation changes if they contain 15 or more individual measurements. First a surface model is fitted to the cell data, using a Levenberg-Marquardt least squares fitting method. The model equation is

$$z(x, y, h) = z_m + a_0x + a_1y + a_2x^2 + a_3y^2 + a_4xy + a_5h + a_6t \quad \text{Equation 2.4}$$

where z is height, x is the polar stereographic easting coordinate, y is the polar stereographic northing coordinate, h is the satellite heading (set as binary), and t is the time of the elevation measurement in years. Measured heights more than two standard deviations from the modelled height are discarded, and this procedure is repeated until either no outliers or fewer than fifteen data points remained (in which case the results in the grid cell were not used).

A second model is then fitted to the slope- and satellite heading-corrected elevation anomalies emerging from each mission plane fit solution to remove residual, short-period fluctuations correlated with changes in backscattered power that arise in radar altimeter measurements over continental ice sheets (Wingham et al., 1998). This model is applied in a separate step to ensure that it does not interfere with the spatial and temporal elevation fit. It is again determined using a Levenberg-Marquardt least squares, with an equation of the form

$$p = a_0 + a_1t + a_2h \quad \text{Equation 2.5}$$

where p is the backscatter power, t is the time of the measurement in years, and h is the satellite heading. A time series of backscatter power is reconstructed using this model fit and the anomalies, and 5-year trends in dp/dz were computed centred on the mid-point of each mission by matching the power and elevation anomaly time-series. These periods are chosen due to their relative stability in terms of orbit manoeuvres, outages and on-board changes. The fitting procedure is again iterated to remove outliers more than two standard deviations from the modelled value, either until there were none or more than three iterations had occurred (in which case the results were not used). As Sentinel-3A and B are recent missions, the power correction can only use two years of their data instead of five.

Finally the measurements are aggregated into 140-day epochs in each satellite mission. In each grid cell, the average residual height within each epoch is calculated using a resistant mean by discarding data more than two standard deviations from the median and compensating for the truncation with an approximation formula. The missions are then cross-calibrated to produce the final timeseries.

2.3.2 Cross-calibration

To produce continuous, multi-mission time-series of height change, biases have to be accounted for between missions. In all cases, the objective is to align ERS-2, Envisat, CryoSat-2 and Sentinel-3 timeseries with ERS-1. First, a model is defined for the shape of each time-series taking the form of a seasonal cycle imposed on a linear gradient. The model equation is

$$z = a_0 + a_1t + a_2 \sin(2\pi t + a_3) \quad \text{Equation 2.6}$$

where z is the height change and t is the average time at each epoch in the series, in years. For each mission, the model coefficients are solved for using a Levenberg-Marquardt least-squares fit applied to sections of data that overlap as far as possible. In most cases these are centred on the mid-times between

one mission's end and the next mission's start dates, but since CryoSat-2 and Sentinel-3A are both simultaneously operative a period near the start of Sentinel-3A's mission is used. The lengths of each section vary due to the duration of the mission overlap and range from 1 to 3.5 years. For each overlapping pair of missions, the bias is then calculated as the median value of the difference between modelled height anomalies over a common, 2-year period, (e.g. figure 2.3, taken from Shepherd et al, 2019).

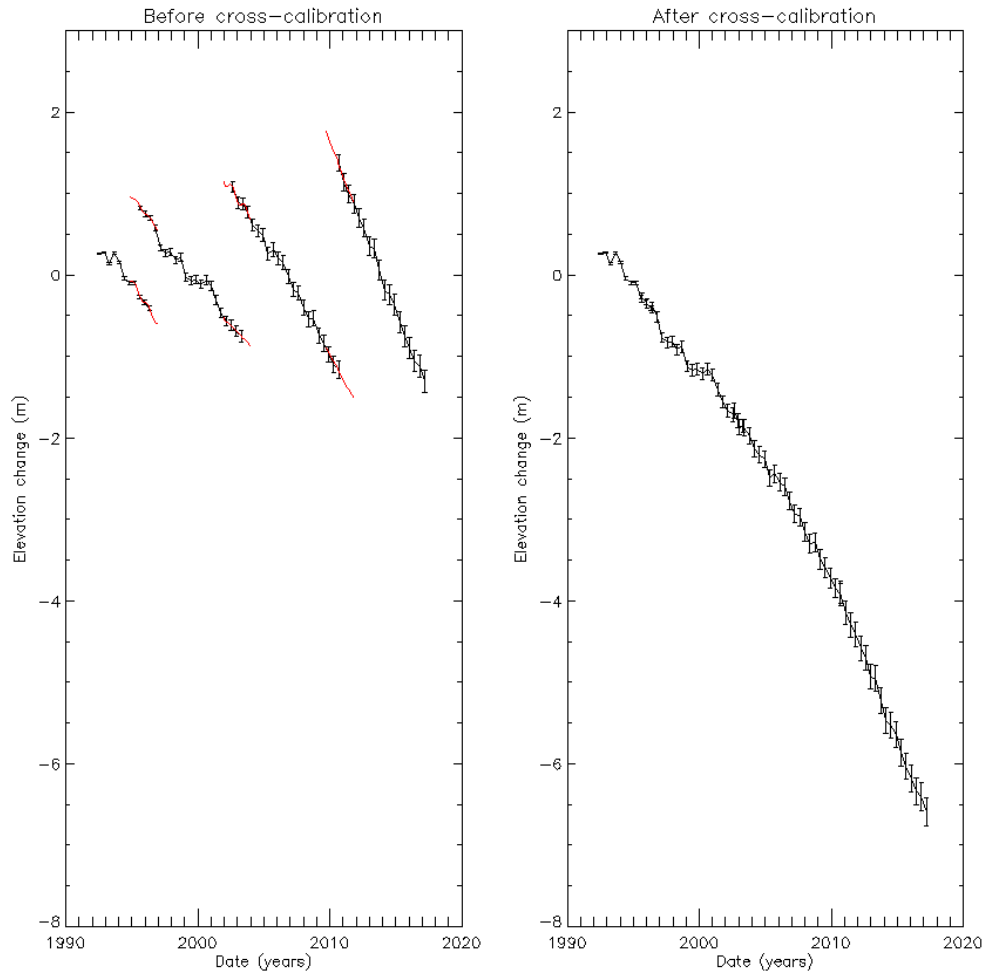


Figure 2.3: Example elevation trends computed from single mission time series (left) and the multi-mission ensemble (right) computed after adjusting for the bias arising at mission overlap periods (shown in red).

The biasing method can be applied to elevation changes within individual grid cells (pixel cross-calibration), and to averages computed over larger regions of interest (termed basin cross-calibration), including areas of ice dynamical imbalance, drainage basins, and ice sheets. The certainties of the bias corrections improve as the area of interest increases due to the volumes of data included in the model fits.

2.4 Input data and algorithm output

The raw elevation data are from radar altimeters mounted on satellites, ERS 1 and 2, Envisat, CryoSat-2 and Sentinel-3. These satellites have provided continuous coverage of the Antarctic ice sheets since May 1992. ERS-1 and ERS-2 data are surfaces flagged as continental ice, when the satellite was in ice tracking mode, from 'Reprocessing of altimeter products for ERS' (REAPER) level 2 data files. Envisat data are

surfaces flagged as continental ice, when the satellite was in 320 Mhz tracking mode, from level 2 radar altimeter geophysical data record v2.1 data files. For all ERS-1, ERS-2, Envisat, Sentinel-3 and CryoSat-2 low resolution model (LRM) data, the altimeter waveforms were processed using a Threshold offset Centre Of Gravity (TCOG) retracker. CryoSat-2 data are surfaces flagged as land/ice from baseline C level 2 low rate mode and synthetic aperture radar interferometry mode data files. Sentinel-3 data is flagged as continental_ice_snow and is overwhelmingly from SAR mode. In each case, the measurements used were time, slope-corrected geographic location, slope- and geophysically-corrected height, backscatter power and orbit heading (ascending or descending). The geophysical corrections used were the dry tropospheric correction, the wet tropospheric correction, the ionospheric correction, the solid Earth tide and the ocean loading tide. All data files except for Envisat's included the geophysical corrections in their height measurements, while for Envisat they were supplied separately and applied during data ingestion. Due to an error in some Envisat data files, a better dry tropospheric correction was obtained from an auxiliary set of point target response files. An external model (Iijima et al., 1999) is used to adjust Envisat data for propagation of the radar signal through the ionosphere after the secondary S-band altimeter failed in 2008. A correction is also applied to all missions' elevation measurements to account for the effects of post-glacial rebound, using the IJ05_R2 model (Ivins et al., 2013).

A generalised scheme for ingestion of from each altimeter is shown in Figure 2.4. The gridded outputs from each altimeter are then cross-calibrated to produce a single, similarly-gridded, output dataset.

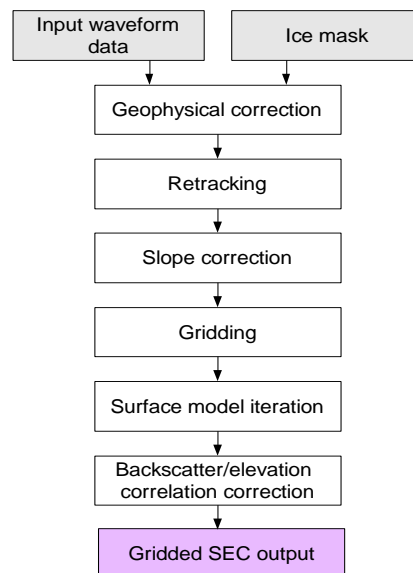
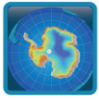


Figure 2.4. Schematic of the plane fit SEC processing line.

2.5 Accuracy and performance

For any given satellite mission, the uncertainty is estimated at each epoch of an elevation change (dz) time series as a combination of systematic and time-varying sources of error. Systematic errors are defined as those that may impact the long-term trend in elevation and are estimated from the standard error of the rate of surface elevation change (dz/dt) that is derived from each respective time series. Sources of systematic error may include spatially coherent changes in elevation that are not represented by the functional form of the surface model, such as short-lived accumulation events or changes driven by snowpack characteristics that are not accounted for by the empirical backscatter model (equation 2.5). It is unlikely that the assumed topography (plane, curved, digital elevation model (DEM), etc.) will perfectly represent the actual topography, and this introduces errors in the derived surface elevation change (SEC). In general, a simple topography applies better to the central, flat areas of the Antarctic ice sheet than the coastal areas characterized by a more complex topography. Therefore, the error is generally larger in



areas with steeper surface slopes. Furthermore, the uncertainty on each individual elevation estimate is also slope dependent (Brenner et al., 2007).

For each time series, the systematic uncertainty is cumulatively summed at each epoch, so that the contribution from this component grows linearly with time. Additional, time varying uncertainty may arise due to errors that affect individual epochs and impinge on the ability to determine the regionally averaged elevation anomaly at that particular time. This term is influenced by factors such as measurement precision and non-uniform spatial sampling, and its influence is quantified based upon the dispersion of contributing measurements at each individual epoch. Specifically, for every epoch within any given time series, the regional average of the standard error of dz measurements within all contributing pixels is computed. In contrast to the systematic term, it is assumed that the time varying component is temporally uncorrelated, and so at any given epoch all preceding epoch uncertainties are added, in quadrature.

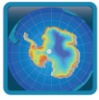
One source of uncertainty which is not reflected by the modelling error estimate is the fact that radar signal penetrates into the snow, and that the penetration depth varies in both space and time, being a function of snow properties. Therefore, it is uncertain exactly how the radar derived SEC relates to the physical snow surface elevation change.

To estimate the cross-calibration uncertainty, the standard deviation of the differences between the modelled elevations from each successive pair of satellite missions is computed. This essentially measures the precision with which the two missions can be aligned, based upon the variance of the respective modelled elevations within the defined overlap period. The biasing uncertainty is set to zero for the first mission in the time series (ERS-1), as by definition no multi-mission adjustment is required, and then increases at each subsequent inter-mission boundary. Specifically, at each epoch the biasing uncertainties arising from all preceding inter-mission overlap periods are summed in quadrature. The total multi-mission uncertainty at each epoch is then computed by summing the single mission uncertainty (described above) and the biasing uncertainty in quadrature. Finally, the uncertainty on the multi-mission rate of elevation change is computed by dividing the total uncertainty accumulated at the end of the time series by the duration of the record, to ensure that all components of the uncertainty budget are taken into account within the resulting trend estimate.

Finally, the systematic and time-varying contributions are summed in quadrature, to determine an estimate of the overall elevation change uncertainty at each epoch.

In the preceding AIS CCI project, agreement between elevation change estimates obtained by the various along-track methods discussed and the crossover analysis demonstrated good performance capabilities of these methods. In another study (Horwath et al., 2012), elevation changes derived from the Envisat over the Antarctic Ice Sheet were compared with results of gravity changes from GRACE. In contrast to Thomas et al. (2008), the comparison showed a good agreement between linear trends and inter-annual variations that reflect surface mass balance changes. Although temporal changes of the surface properties are more pronounced in Greenland than in Antarctica, this result confirms the ability of radar altimetry to provide reasonable elevation change estimates.

In Antarctica the largest areas of known mass imbalance are over the continental glacial margins, and particularly of West Antarctica and the Antarctic Peninsula, mountainous areas of high slope and rough terrain. These are relatively poorly sampled by the tracking capabilities and orbital pattern of traditional pulse limited altimeter missions. However, CryoSat-2 with its interferometric SAR mode and improved spatial sampling of its orbit allows a dense survey of these regions. Comparison of elevation changes derived from CryoSat data using the plane fit method against results derived from airborne laser altimetry over the Amundsen Sea Sector of West Antarctica (McMillan, et al., 2014) where rates of ice thickness change are varied and large show that CryoSat measurements are in close agreement with these airborne observations. After adjusting for bias introduced by the airborne sampling pattern, the mean difference (31 cm yr⁻¹) is smaller than the expected elevation fluctuation due to snowfall variability.



2.6 Capabilities and known limitations

The main advantages of the along track methods are an increased quantity and spatial distribution of elevation change measurements in comparison to the crossover method, again see the preceding AIS CCI project ATBD. They increase the SNR of the analysis and the spatial resolution of the measurements. The gridding allows the capture of local scale phenomena much better than the sparse crossover points. One disadvantage when using radar altimetry over ice sheets is that the radar-tracked surface changes with time; the penetration depth of the radar depends on the surface state. The measured height is then variable according to surface state variations or other volume echo intensity variations (linked to temperature changes impacting the medium's absorption). A disadvantage of the plane fitting method is that the potential elevation change signal between the two repeat tracks is present in the reference plane.

The elevation-change timeseries survey the majority of the continental ice sheet area falling within the satellite orbital limits, but some places are omitted where gaps arise between the satellite ground tracks, where the altimeters fail to track rugged terrain, and where the mission cross calibration locally fails. This region includes some ice marginal areas due to the northwards broadening of ground track spacing. The largest single area of data omission is the region south of the satellite orbital limits, 88°S for CryoSat-2 and 81.5°S for the other missions.

2.7 References

Bamber, J.L. (1994). Ice sheet altimeter processing scheme, *Int. J. Remote Sensing* 15, 4, 925-938.

Brenner, A.C., J.P. DiMarzio, and H.J. Zwally, (2007). Precision and accuracy of satellite radar and laser altimeter data over the continental ice sheets, *IEEE Trans. Geosci. Remote Sens.* 45, 2, 321-331.

Cornford et al (2013), Adaptive mesh, finite volume modelling of marine ice sheets, *Journal of Computational Physics*, 232(1):529-549.

Davis, C.H. and A.C. Ferguson (2004). Elevation change of the Antarctic ice sheet, 1995-2000, from ERS-2 satellite radar altimetry, *IEEE Trans. Geosci. Remote Sens.* 42, 11, 2437-2445.

Davis, C.H. and V.I. Poznyak (1993). The depth of penetration in Antarctic Firn at 10 Ghz, *IEEE Trans. Geosci. Remote Sens.* 31, 5, 1107-1111.

Davis, C.H. (1997). A robust threshold retracking algorithm for measuring ice sheet surface elevation change from satellite radar altimeters, *IEEE Trans. Geosci. Remote Sens.* 35, 4, 974 - 979.

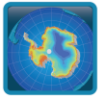
Davis, C.H., Y. Li, J.R. McConnell, M.M. Frey and E. Hanna (2005). Snowfall-driven growth in East Antarctic ice sheet mitigates recent sea-level rise, *Science* 308, 5730, 1898-1901.

Elachi, C. (1988). *Spaceborne Radar Remote Sensing: Applications and Techniques*, IEEE Press, New York.

ESA Climate Change Initiative, Essential Climate Variable, Antarctic Ice Sheet, Algorithm Theoretical Basis Document (2017) ST-UL-ESA-CCIAIS-ATBD-001v3

Ferguson, A.C., C.H. Davis and J.E. Cavanaugh (2004) An autoregressive model for analysis of ice sheet elevation change time series, *IEEE Trans. Geosci. Remote Sens.* 42, 11, 2426-2436.

Fu, L.L. and A. Cazenave (2001). *Satellite Altimetry and Earth Sciences: A Handbook of Techniques and Applications*. International Geophysics Series Vol. 69, Academic Press, San Diego, 457 pp.



Ewert, H, Groh, A and Dietrich, R. (2012). Volume and mass changes of the Greenland ice sheet inferred from ICESat and GRACE, *Journal of Geodynamics*, 59-61.

Horwath, M., B. Legresy, F. Remy, F. Blarel, and J. Lemoine (2012). Consistent patterns of Antarctic ice sheet interannual variations from ENVISAT radar altimetry and GRACE satellite gravimetry, *Geophys. J. Int.* 189, 863–876.

Howat, I. M., B.E. Smith, I. Joughin, and T.A. Scambos (2008). Rates of Southeast Greenland ice volume loss from combined ICESat and ASTER observations, *Geophys. Res. Lett.* 35, L17505.

Johannessen, O.M., K. Khvorostovsky, M.W. Miles and L.P. Bobylev (2005). Recent ice-sheet growth in the interior of Greenland, *Science* 310, 5750, 1013–1016.

Khvorostovsky, K. (2011). Merging and analysis of elevation time series over Greenland ice sheet from satellite radar altimetry, *IEEE Trans. Geosc. Remote Sens.* 50, 1, 23-36.

Legrésy B. and F. Rémy (1998). Using the temporal variability of satellite radar altimetric observations to map surface properties of the Antarctic ice sheet, *J. Glaciol.* 44, 147, 197–206..

Legrésy, B., F. Papa, F. Rémy, G. Vinay, M. Van den Bosh and O.Z. Zanife (2005). ENVISAT radar altimeter measurements over continental surfaces and ice caps using the ICE-2 retracking algorithm, *Remote Sensing of Environment* 95, 150–163.

Li, Y. and C.H. Davis (2006). Improved methods for analysis of decadal elevation change time series over Antarctica, *IEEE Trans. Geosc. Remote Sens.* 44, 10, 2687–2697.

McMillan, M., A. Shepherd, A. Sundal, K. Briggs, A. Muir, A. Ridout, A. Hogg and D. Wingham (2014). Increased ice losses from Antarctica detected by CryoSat-2, *Geophys. Res. Lett.* 41, 11, 3899-3905.

Moholdt, G., J.O. Hagen, T. Eiken and T.V. Schuler (2010a). Geometric changes and mass balance of the Austfonna ice cap, Svalbard, *The Cryosphere* 4, 21–34.

Moholdt, G., C. Nuth, J.O. Hagen and J. Kohler (2010b). Recent elevation changes of Svalbard glaciers derived from ICESat laser altimetry, *Remote Sensing of Environment* 114, 2756–2767.

Daniele Fantin, et al., (2015). Algorithm Theoretical Basis Document (ATBD) for CCI+ Phase 1 for the ice sheets CCI project of ESA's Climate Change Initiative, version 1.0

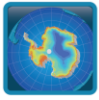
Pritchard, H. D., R.J. Arthern, D.G. Vaughan and L.A. Edwards (2009). Extensive dynamic thinning on the margins of the Greenland and Antarctic ice sheets, *Nature* 461, 971–975.

REAPER REA-UG-PHB-7003 Product Handbook Issue: 2.2 Date: 12/05/2014

Ridley, J. K. and K. C. Partington (1998). A model of satellite radar altimeter return from ice sheets, *Int. J. Remote Sensing* 9, 4, 601424.

Shepherd et al (2019), Trends in Antarctic Ice Sheet Elevation and Mass, *GRL* 46 (14) 8174-8183

Slobbe, D.C., R.C. Lindenbergh and P. Ditmar (2008). Estimation of volume change rates of Greenland's ice sheet from ICESat data using overlapping footprints, *Remote Sensing of Environment* 112, 4204–4213.



Sørensen, L.S., S.B. Simonsen, K. Nielsen, P. Lucas-Picher, G. Spada, G. Adalgeirsdottir, R. Forsberg and C.S. Hvidberg, (2011). Mass balance of the Greenland ice sheet (2003–2008) from ICESat data – the impact of interpolation, sampling and firn density, *The Cryosphere* 5, 173–186.

Thomas, R.H., C.H. Davis, E. Frederick, W. Krabill, Y. Li, S. Manizade and C. Martin (2008). A comparison of Greenland ice sheet volume changes derived from altimetry measurements, *J. Glaciol.* 54, 185, 203–212.

Ulaby, F. T., R.K. Moore and A.K. Fung (1982). *Microwave remote sensing: active and passive*, Addison-Wesley Publishing Company, London.

Whitehouse, P. (2009). . 2009;105, <http://www.skb.se/upload/publications/pdf/TR-09-11.pdf>.

Wingham, D.J., A.L. Ridout, R. Scharroo, R.J. Arthern and C.K. Shum (1998). Antarctic elevation change from 1992 to 1996, *Science* 282, 5388, 456–458.

Wingham, D.J., D.W. Wallis and A. Shepherd. (2009). Spatial and temporal evolution of Pine Island Glacier thinning, 1995-2006, *Geophys. Res. Lett.* 36,

Zlotnicki, V., L.L. Fu and W. Patzert. (1989) Seasonal Variability in Global Sea Level Observed with Geosat Altimetry, *J. Geophys. Res.* 94, C12, 17959-17969,

Zwally, H.J. and A.C. Brenner (2001). Ice sheet dynamics and mass balance, In: Fu, L.L. and A. Cazanave (eds.) *Satellite altimetry and earth sciences*, New York, Academic Press Inc., 351–369.

Zwally, H. J., R. A. Bindschadler, A. C. Brenner, T. V. Martin, and R. H. Thomas. (1983). Surface elevation contours of Greenland and Antarctic ice sheets, *J. Geophys. Res.*, Vol 88, No. C3, pages 1589-1596

Zwally, H.J. (1989). Growth of Greenland ice sheet: interpretation, *Science* 246, 4937, 1589–1591.

Zwally, H.J., J. Li, A.C. Brenner, M. Beckley, H.G. Cornejo, J. DiMarzio, M.B. Giovinetto, T. Neumann, J. Robbins, J.L. Saba, D. Yi and W. Wang. (2011) Greenland ice sheet mass balance: distribution of increased mass loss with climate warming; 2003- 07 versus 1992–2002, *J. Glaciol.* 57, 201, 88–102.

Zwally, H.J., M.B. Giovinetto, J. Li, H.G. Cornejo, M.A. Beckley, A.C. Brenner, J.L. Saba & D. Yi (2005) Mass changes of the Greenland and Antarctic ice sheets and shelves and contributions to sea-level rise: 1992–2002, *J. Glaciol.* 51, 175, 509–527.



3 Ice Velocity

3.1 Introduction

SAR based ice velocity measurements are sensitive to vertical displacements of the reflecting surface due to the nature of the side looking acquisition geometry (Figure 3.1). If observed from the same point in orbit, a vertically displaced object $P_{x,y}$ will be detected closer or further away from the sensor since only the distance in slant range can be detected. The magnitude of the observed slant range displacement Δ_{sr} depends additionally on the local incidence angle θ .

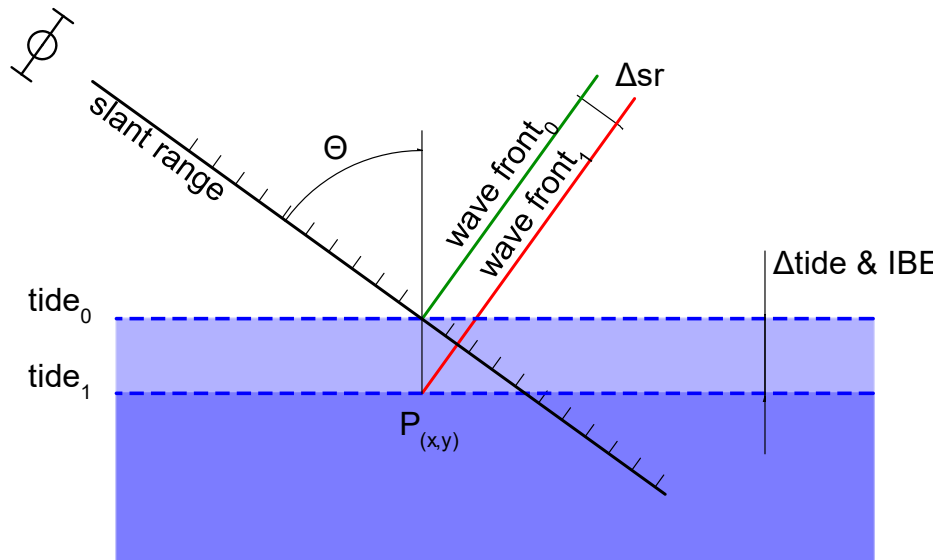


Figure 3.1: Imaging geometry of side looking spaceborne SAR. A vertical displacement of a Point $P_{x,y}$ is imaged at different slant range position (Δ_{sr}) depending on its elevation.

For floating ice, the major contribution to vertical displacement are:

- **Tides**

Under most ice shelves surrounding Antarctica the typical peak-to-peak tidal ranges are $\sim 1-2$ m. At spring tides this values can increase to 2-4 m and occasionally can exceed 6 m (Padman *et al.*, 2002).

- **Inverted Barometric Effect (IBE)**

During a passage of an energetic polar low a surface pressure change of ~ 40 hPa results in vertical displacement of ~ 40 cm of sea surface height (Padman *et al.*, 2003). This value is generally smaller than the daily mean tide level of ~ 2 m but larger than the typical tide model error which is in the order of 10 cm. Therefore IBE is the second largest contribution to the changing sea surface height (Padman *et al.*, 2003).

The presented processing line models these vertical displacements and compensates for the contribution to the ice velocity. The impact of the tides and IBE is clearly visible in the spread of the ice velocities at Demorest Glacier, Larsen-C, from Oct. 2015 – Oct. 2017 (Figure 3.2).

The tool is designed to be extendable to newer tide models and reanalysis data/ data sources.

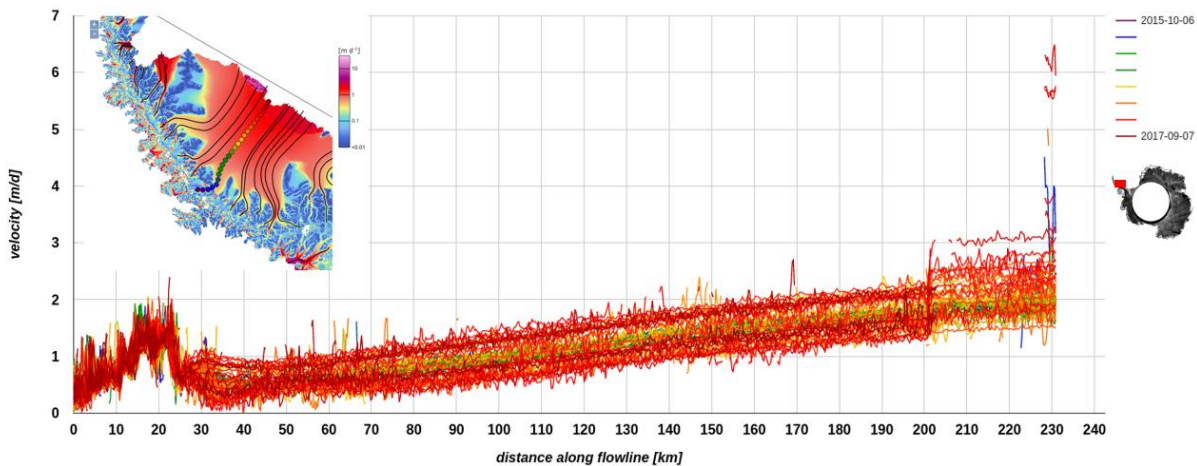
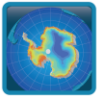


Figure 3.2 Sentinel-1 velocity profiles along Demorest Glacier, Larsen-C, from Oct. 2015 – Oct. 2017 clearly showing the effect of the vertical displacement of the iceshelf, due to tides and atmospheric pressure.

3.2 Review of scientific background

Add justification and importance of tidal correction for ice velocity estimation.

(McMillan et al., 2011) compared three tide models (TPX07.1, CATS2008a_opt and FES2004) in the Amundsen Sea with satellite based InSAR measurements from ERS-1/2 and compensated for the tidal displacement. The selected models perform comparably well with an RMSE of ~ 9 cm. The further inclusion of an atmospheric model improved the tide model predictions by $6\sim\%$. It was concluded that the applied correction can compensate for a velocity error of ~ 22 m/yr in the ground range component of the ice velocity field. In a similar approach (Wild, Marsh and Rack, 2019) validated satellite based DInSAR measurements from TerraSAR-X against GPS data collected on Darwin Glacier, draining from the Transantarctic Mountains to the Ross Sea. The DInSAR measurements were used to improve the tide model (TPX07.1) output by up to 39% from 10.8 to 6.7 cm RMSE against GPS at locations where the ice is in its local hydrostatic equilibrium. For the IBE was accounted.

IBE corrections are justified for atmospheric pressure variations occurring with a frequency of 0.03 to 0.5 cycle per day (Padman et al., 2003) and reduce the standard deviation of the ice-shelf surface elevation from ~ 9 cm to ~ 3 cm.

At the transition zones from grounded to floating ice tidal displacement profiles derived from GPS at Rutherford Ice Stream and Ronne Ice Shelf (Vaughan, 1995) indicated that the flexure can be modelled by an elastic beam model with a single value for the elastic modulus (0.88 ± 0.35 GPa).

3.3 Algorithms

The processing chain to correct for tide and atmospheric pressure induced ice velocity variations is illustrated in Figure 3.3. Input to the algorithm are the uncorrected iv-maps in SAR geometry on burst level, a digital elevation model covering the area of interest, a binary mask identifying the grounded ice as well as tide models and atmospheric reanalysis datasets. First the tidal difference between the acquisition dates of the image pair forming the iv-map is modelled, as well as the surface pressure difference. These model outputs are transformed into SAR geometry. In the second step the elastic beam model (Vaughan, 1995) is applied to the binary mask. Finally, the IV-correction is computed using the geometric relations of the acquisition geometry depicted in Figure 3.1.

Details on each step performed are described in the following subsections.

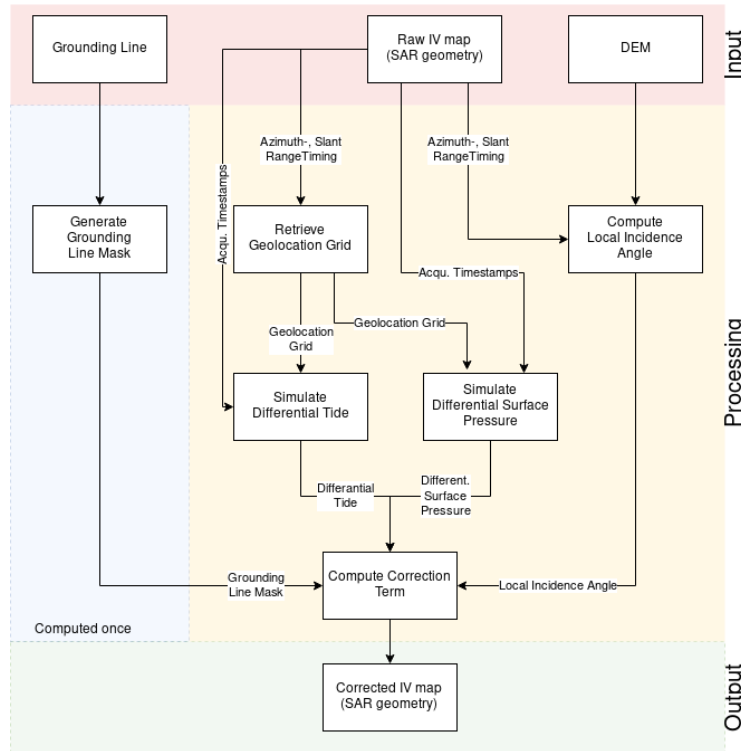


Figure 3.3 High level processing for compensating ice velocity variations induced by tides and inverse barometric effect

Note: In the equations bold symbols s refer to data arrays in SAR -geometry and vectors \vec{s} are marked by an arrow. Quantities are represented in SI units or derived SI units.

3.3.1 Generation of Groundline Mask

To correct ice velocities of the floating ice and ensure a smooth transition to the grounded ice a proximity weighted mask w is created, following (Vaughan, 1995):

$$w = A_0(t) \cdot [1 - e^{-\beta x}(\cos\beta x + \sin\beta x)] \quad \text{Equation 3.1}$$

$$\beta^4 = 3\rho_{sea}g \frac{1 - \nu^2}{Eh^3} \quad \text{Equation 3.2}$$

Where

- $A_0(t)$ is the tidal displacement of the ice surface from its mean position here set to 1 m
- β spatial wave number [m^{-1}] incorporating the spatial frequency of the flexure and its decay length,
- x is the distance orthogonal to the grounding line in meter
- ρ_{sea} is the density of the sea water 1030 kg/m^3
- g the gravitational acceleration 9.81 m/s^2 ,
- E is Young's modulus, set to 0.88 GPa,
- ν is Poissons's ratio set to 0.3 and
- h the thickness of the ice shelf approximated with 500 m.



The mask w reflects the deformation response to tidal forcing. It scales from 0 inland and grounded ice to 1 on open water and floating ice and reaches a maximum value of 1.043 at a distance ~ 4500 m off the grounding line (Figure 3.4) with the above stated parameters.

This mask is created once for entire Antarctica in geographic coordinates.

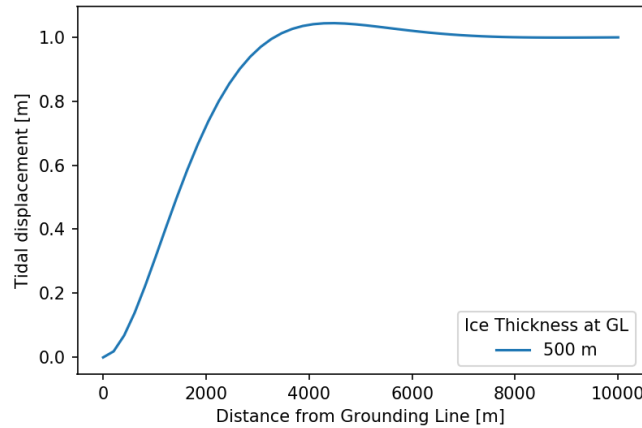


Figure 3.4: Vertical displacement response of a 500m thick ice shelf to tidal forcing.

3.3.2 Retrieve Geolocation Grid

In order to employ the tide model and IBE corrections the area covered by the SAR image must be recovered from the slant and azimuth timestamps. This procedure, the forward geocoding, involves a DEM to extract the latitude longitude geolocation grid (GG) covered by the SAR scene (Small and Schubert, 2019).

This step is performed each SAR iv map.

3.3.3 Compute Local Incidence Angle

The local incidence angle θ is derived by computing the dot product between unit vector of the line of sight vector \vec{u}_{los} and the normal vector \vec{n}_{DEM} to the point of interest in the DEM identified by the GG.

$$\theta = \text{acos}(\vec{u}_{los} \cdot \vec{n}_{DEM}) \quad \text{Equation 3.3}$$

This step is performed each SAR iv map.

3.3.4 Simulation of differential Tide

To model tides the Python module pyTMD (available at: <https://github.com/tsutterley/pyTMD>) and tide OSU (Oregon State University, USA) tide models files (available at <https://www.tpxo.net>) are utilized.

The GG containing the geographic location of every SAR pixel is passed together with the acquisition timestamp to the Python module pyTMD toolbox where the tide for the master and the slave acquisition date is simulated. The tidal prediction is based on Laplace's tidal equations and evaluated with the following harmonic constituents:



Table 3.1 Selected tidal constituents applied in the Tidal Prediction Software

Semi-diurnal	Symbol
Principal lunar semidiurnal	M2
Principal solar semidiurnal	S2
Larger lunar elliptic semidiurnal	N2
Lunisolar semidiurnal	K2
Diurnal	Symbol
Lunar diurnal	K1
Lunar diurnal	O1
Solar diurnal	P1
Larger lunar elliptic diurnal	Q1
Long period	Symbol
Lunisolar fortnightly	Mf
Lunar monthly	Mm
Short period (nonlinear)	Symbol
Shallow water overtides of principal lunar	M4
Shallow water quarter diurnal	MS4
Shallow water quarter diurnal	MN4

The tidal maps contain the tidal elevations ssh computed with the constituent of Table 3.1 with respect to the mean sea level (MSL) at a given time. The tidal difference Δssh at a position \vec{P} (latitude, longitude) is given by:

$$\Delta ssh = ssh(t_1, \vec{P}) - ssh(t_0, \vec{P}) \quad \text{Equation 3.4}$$

Where t_0 reflects the acquisition time of the master scene and t_1 the acquisition time of the slave scene forming the image pair for iv retrieval.

This step is performed each SAR iv map.

3.3.5 Simulation of differential Surface pressure

Between two SAR acquisitions t_0 and t_1 the atmospheric pressure exerted on the ocean surface varies causing the local sea surface topography to deform which is known as the inverted barometric effect. A change in 10 hPa in surface air pressure, results in a change of 10 cm at sea level (Equation 3.5). This vertical displacement causes a range distance change.

$$c_{IBE} = -10^{-5} \text{ [m/Pa]} \quad \text{Equation 3.5}$$

In order to compensate for the IBE the surface pressure p_{sfc} is retrieved from ERA5 Reanalysis dataset. It contains surface pressure data reanalysed 4-times daily. The surface pressure $p_{sfc}(t, \vec{P})$ for the acquisition dates t_0 and t_1 are linearly interpolated between the adjacent dataset layer at position \vec{P} provided in the GG. For the further processing the surface pressure difference Δp_{sfc} is formed with Equation 3.6.

$$\Delta p_{sfc} = p_{sfc}(t_0, x) - p_{sfc}(t_1, x) \quad \text{Equation 3.6}$$

This step is performed each SAR iv map.

3.3.6 Correction of atmospheric and tidal induced iv variations

To the uncorrected ice velocity map iv_{uncorr} a correction term accounting for the tides and the IBE is added. From vertical tidal displacement Δssh (Equation 3.4) the vertical displacement attributed to IBE is added according to Equation 3.5 and Equation 3.6. The displacement is projected into SAR geometry by multiplying the product by the cosine of the incidence angle θ and further dividing it by the slant range pixel spacing sz_{rg} . Applying the mask w to the product ensures a smooth transition in ice velocity from grounded to floating ice. In the last step the displacement is normalized with the time lag between the two acquisitions to arrive at the ice velocity correction term.

$$iv_{corr} = iv_{uncorr} + \left(\frac{(\Delta ssh + \Delta p_{sfc} c_{IBE}) \cos(\theta) w}{sz_{rg}} \right) \frac{1}{(t_1 - t_0)} \quad \text{Equation 3.7}$$

This step is performed each SAR iv map.

3.4 Input data and algorithm output

The following input data sets are required to run the tidal correction algorithm:

- Uncorrected iv-map in SAR geometry at burst level
- Tide Model
- Mask of grounded ice
- Reanalysis data of surface pressure
- Digital Elevation Model (DEM)

3.4.1 Uncorrected iv-map in SAR geometry at burst level

The software takes uncorrected iv maps in SAR geometry at burst level as an input with the ice velocities given in meters per day. The availability of the state vector information azimuth and slant range timing is essential to the processing.

3.4.2 Tide Model

The tide model CATS2008: Circum-Antarctic Tidal Simulation version 2008 (CATS2008; Erofeeva et al., 2019) is a regional ocean tide model. It has a resolution of 4 km within the bounds West: -180, East: 180, South: -90, North: -40.231. The polar stereographic grid is centred at 71 degrees S, 70 degrees W. The provided constituents are: M2, S2, N2, K2, K1, O1, P1, Q1, Mf and Mm.

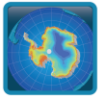
The coastline is based on the MODIS Mosaic of Antarctica (Scambos *et al.*, 2007) feature identification files, adjusted to match ICESat-derived grounding lines for the Ross and Filchner-Ronne ice shelves and Interferometric Synthetic Aperture Radar (InSAR) grounding lines.

Satellite altimetry data was used to best-fit the Laplace Tidal Equations in the least squares sense and obtain the model (Data access: <https://www.usap-dc.org/view/dataset/601235>).

As CATS2008 has the most accurate grounding line position it was selected for this project.

3.4.3 Mask of Grounded Ice

The basis for the mask ensuring a smooth transition in the ice velocity field is derived from MEaSUREs Grounding Line dataset (Mouginot, 2017). It comprises grounding line locations between 1992 and 2015 distributed as ESRI shapefiles (Data access: <https://nsidc.org/data/nsidc-0709>).



Differential satellite synthetic aperture radar interferometry (DInSAR) was used to derive the grounding line location. Data sources are:

- Earth Remote Sensing Satellites 1 and 2 (ERS-1 and -2)
- RADARSAT and RADARSAT-2
- Advanced Land Observing System (ALOS)
- PALSAR for years 1992 to 2009
- Copernicus Sentinel-1A for years 2014 to 2015.

3.4.4 Reanalysis Data of Surface Pressure

ERA5 is the fifth generation ECMWF atmospheric reanalysis of the global climate. ERA5 provides hourly estimates of variables on pressure levels on a global grid with a spatial resolution of $0.25^{\circ} \times 0.25^{\circ}$ (C3S, 2017). ERA5 better resolves smaller scale differences improving the IBE correction. ERA5 is freely available within 5 days of real time through the Copernicus Climate Data Store (<https://cds.climate.copernicus.eu/>).

3.4.5 Digital Elevation Model

The Reference Elevation Model of Antarctica (REMA) is a DEM covering Antarctica with a resolution of less than 10 m and a typical elevation error of less than 1 m with respect to airborne laser altimetry. It was created from stereoscopic imagery collected by WorldView-1, WorldView-2, WorldView-3, and GeoEye-1 with the mean acquisition date 9 May 2015 and a standard deviation of 432 days (Howat *et al.*, 2019).

In this project it was decided to utilize the reduced-resolution resampled version with a pixel spacing of 200 m. (Data access: <http://data.pgc.umn.edu/elev/dem/sets/REMA/>)

3.5 Accuracy and performance

The potential of the ice velocity correction for known atmospheric and tidal effects is discussed in this section on the example of Anderson Glacier at Larsen C (Antarctic Peninsula). Data available at: <https://cryoportal.enveo.at/>.

In the comparison illustrated in Figure 3.5 ice velocity is color-coded in the overview ranging from 0.2 m/day inland to ~ 1.5 m/day on the floating ice. The comparison is performed along the flowline in steps of 5 km starting inland. Basis of the depicted mean ice velocity map are 39 individual ice velocity maps formed by Sentinel-1 image pairs with a temporal baseline of 6 days acquired between 01. 01. 2017 and 28. 09. 2017 shown in the blueish boxplot. The box extends from the lower to upper quartile values of the data, with a line at the median. The whiskers extend to show the range of the ice velocity at the corresponding point. Tidal and IBE correction were applied to the same stack of ice velocity maps resulting in the green boxplots of Figure 3.5. The reduction in the error bar is clearly visible for regions on the floating ice (points 35 km to 220 km). At the transition zone (point 30 km) the correction degrades the ice velocity estimate, indicating that the ice at this location is grounded and therefore the mask does not reflect the grounding line position properly. Further upstream the ice is grounded.

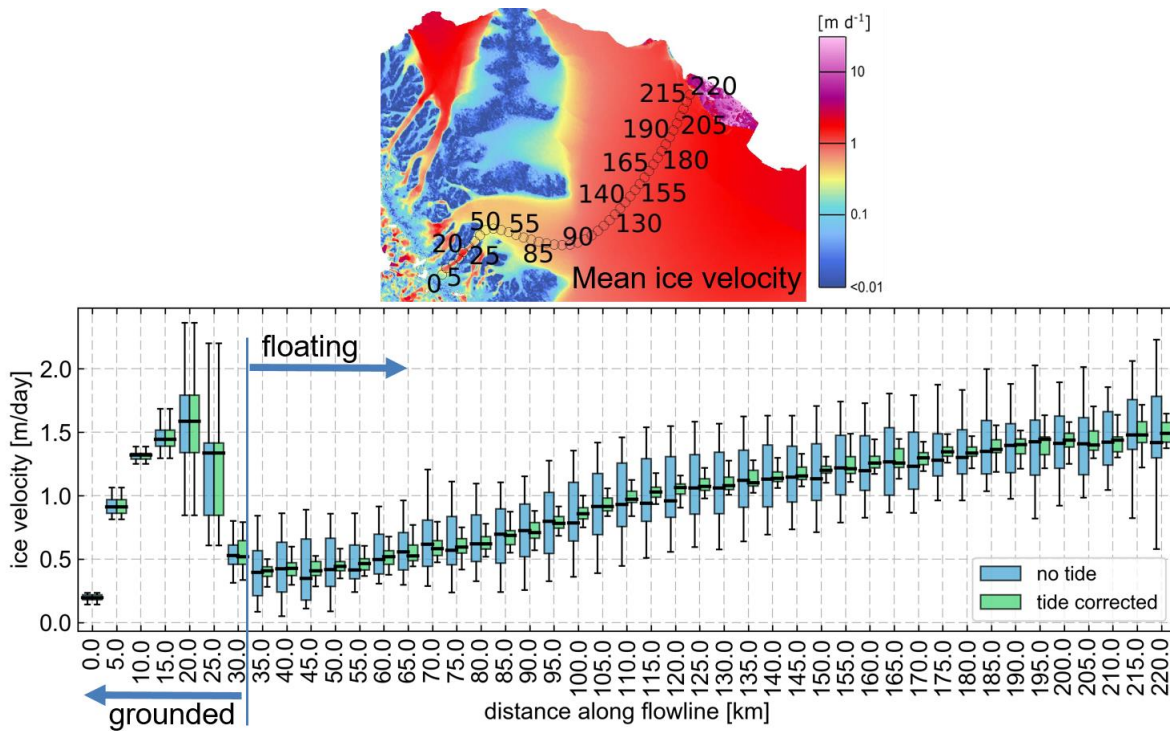


Figure 3.5: Comparison of corrected and uncorrected ice velocity maps at Anderson Glacier, Larsen C, justifying the tidal and IBE correction.

3.6 Capabilities and known limitations

In addition to the limitation inherent to the ice velocity maps derived from satellite-based SAR systems the following limits should be considered:

Limitation of tide models:

- Tide models neglect ice dynamics at the grounding zone
- Tide model might have inaccurate water column thickness underneath the ice shelf
- Unmodeled effects on sea level-height such as mean dynamic topography and storm surges

Limitation of reanalysis data:

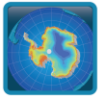
- Temporal and spatial resolution

Grounding line location:

- Uncertainties in the grounding line position and therefore effects along grounding zone.

Method:

- Modelling the tidal flexure zone with the elastic beam model holds for regions with relatively steep bedrock, where the grounding line does not migrate during the tidal cycle. At locations with shallow bedrock slope the grounding line migrates therefore reduces the bending stress in the ice sheet and modifying the geometry at the hinging zone (Vaughan, 1995).
- Smaller ice shelves show a stronger response (~ -0.93 cm/hPa) to IBE compared to large ice shelves with a value of -0.88 to -0.90 cm/hPa (King *et al.*, 2011)



3.7 References

- Erofeeva, S., Howard, S. L. and Padman, L. (2019) 'CATS2008: Circum-Antarctic Tidal Simulation version 2008'. U.S. Antarctic Program (USAP) Data Center. doi: 10.15784/601235.
- Howat, I. M. et al. (2019) 'The Reference Elevation Model of Antarctica', *The Cryosphere*, 13(2), pp. 665–674. doi: 10.5194/tc-13-665-2019.
- King, M. A. et al. (2011) 'Ocean tides in the Weddell Sea: New observations on the Filchner-Ronne and Larsen C ice shelves and model validation', *Journal of Geophysical Research*, 116(C6), p. C06006. doi: 10.1029/2011JC006949.
- McMillan, M. et al. (2011) 'Tide model accuracy in the Amundsen Sea, Antarctica, from radar interferometry observations of ice shelf motion', *Journal of Geophysical Research*, 116(C11), p. C11008. doi: 10.1029/2011JC007294.
- Mouginot, J. (2017) 'MEaSURES Antarctic Boundaries for IPY 2007–2009 from Satellite Radar, Version 2'. NASA National Snow and Ice Data Center DAAC. doi: 10.5067/AXE4121732AD.
- Padman, L. et al. (2002) 'A new tide model for the Antarctic ice shelves and seas', *Annals of Glaciology*, 34, pp. 247–254. doi: 10.3189/172756402781817752.
- Padman, L. et al. (2003) 'Ice-shelf elevation changes due to atmospheric pressure variations', *Journal of Glaciology*, 49(167), pp. 521–526. doi: 10.3189/172756503781830386.
- Scambos, T. A. et al. (2007) 'MODIS-based Mosaic of Antarctica (MOA) data sets: Continent-wide surface morphology and snow grain size', *Remote Sensing of Environment*, 111(2–3), pp. 242–257. doi: 10.1016/j.rse.2006.12.020.
- Small, D. and Schubert, A. (2019) 'Guide to Sentinel-1 Geocoding'. University of Zurich / RSL. Available at: <https://sentinel.esa.int/documents/247904/1653442/Guide-to-Sentinel-1-Geocoding.pdf> (Accessed: 2 June 2019).
- Vaughan, D. G. (1995) 'Tidal flexure at ice shelf margins', *Journal of Geophysical Research: Solid Earth*, 100(B4), pp. 6213–6224. doi: 10.1029/94JB02467.
- Wild, C. T., Marsh, O. J. and Rack, W. (2019) 'Differential interferometric synthetic aperture radar for tide modelling in Antarctic ice-shelf grounding zones', *The Cryosphere*, 13(12), pp. 3171–3191. doi: 10.5194/tc-13-3171-2019.

4 Appendix 1 – Round Robin Ice Velocity on Ice Shelves

4.1 Introduction

For IV-tidal correction a Round Robin (RR) was designed and conducted, in which experts in the field of IV retrieval were invited to participate. The principal goal of the RR was to intercompare and determine the most suitable approach for correction of tidal influences on ice velocities for ice shelves. As test region the Larsen-C Ice Shelf in the Antarctic Peninsula was selected. The tidal range in this region is in the order of ± 2 m leading to large biases in the derived ice velocities (Figure 3.2). For the RR all participants were provided with a RR package, containing Sentinel-1 SAR data covering the ice shelf for a period of approximately 1 month (or one full tidal cycle) in January/February 2019; a DEM and precise orbit files. The participants were asked to use this data set and provide velocity maps for each repeat pair during the period (in total 5) with and without tidal correction applied and geocoded on a uniform 200 m grid spacing. Additionally, all participants were asked to fill in a feedback/response form to specify software and processing details. Of the (five) RR invitees, three groups responded and participated in the exercise, apart from WP lead ENVEO, these included DTU and DLR, both partners in the project. The results were intercompared on a pixel-by-pixel level for both velocity components and also with a reference map. The reference map was compiled from longer-term averaged ice velocity (6-months) centred on the RR SAR acquisition dates (Oct 2018-Mar 2019). In addition, two tide models and surface pressure reanalysis data sets were intercompared using the RR data sets. This Appendix provides the main outcome of the RR intercomparison exercise and forms the basis for the tidal correction algorithm selection.

4.2 Test Area & Reference Velocity

The Larsen C Ice Shelf in the Antarctic Peninsula was selected as test area for the RR experiment. This area is of primary interest as nearby ice shelves, further north, have all collapsed in recent decades leading to a significant acceleration of their tributary glaciers continuing in to the present (Rott et al., 2018). Larsen C is also the birthplace of the massive iceberg (A-68) which calved off in July 2017, reducing the ice shelf area by more than 12% and presenting a significant risk to its stability (Jansen et al., 2015). At present the time series of Sentinel-1 IV maps in this area spans well over 5 years. However preliminary analysis of the IV time-series revealed specific limitations that needed to be addressed. In particular, the short-term IV retrieval over the ice shelf is strongly affected by tidally induced motion, which has an amplitude of approximately 2m (see Figure 3.2 and Figure 4.1). The vertical displacement between the repeat acquisitions introduces an error in the horizontal velocity that hampers the identification of dynamical signals due to for example ungrounding through basal melt and/or iceberg calving. The Larsen C case is reminiscent for ice shelves elsewhere in Antarctica with large tidal fluctuations.

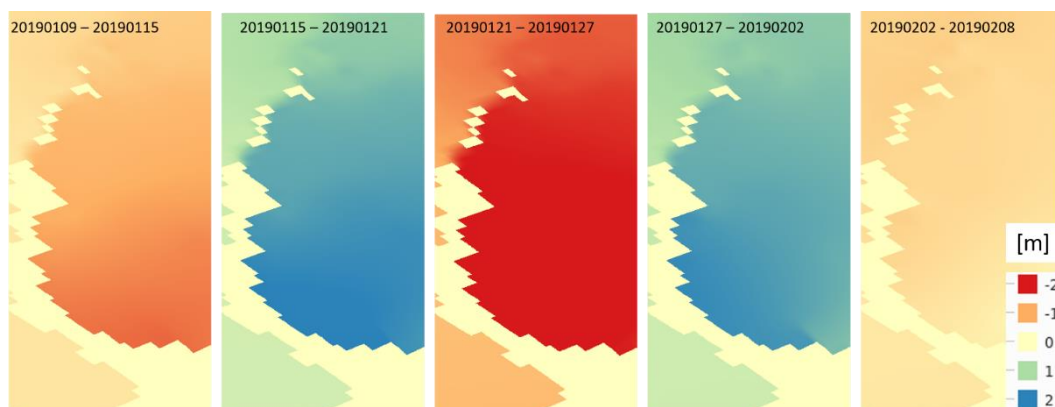
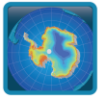


Figure 4.1: Tidal Difference between Sentinel-1 image pairs



Unfortunately, despite the many science expeditions that have visited Larsen C Ice Shelf in recent years, only little contemporaneous in-situ GPS data is acquired which is suitable as a reference dataset for the RR exercise. We have contacted several field teams, including from the project MIDAS field campaigns, to inquire about the availability but they reported catastrophic equipment failure with all three stations recording less than 20 minutes of data (Adam Booth, Adrian Luckman, Pers. Comm.). Instead, a 6-month averaged ice velocity map was generated, based on Sentinel-1 monthly ice velocity maps generated at ENVEO (Figure 4.2). The time frame was selected to be centred on the period of the RR (Jan 2019) and spanned the months October 2018-Mar 2019.

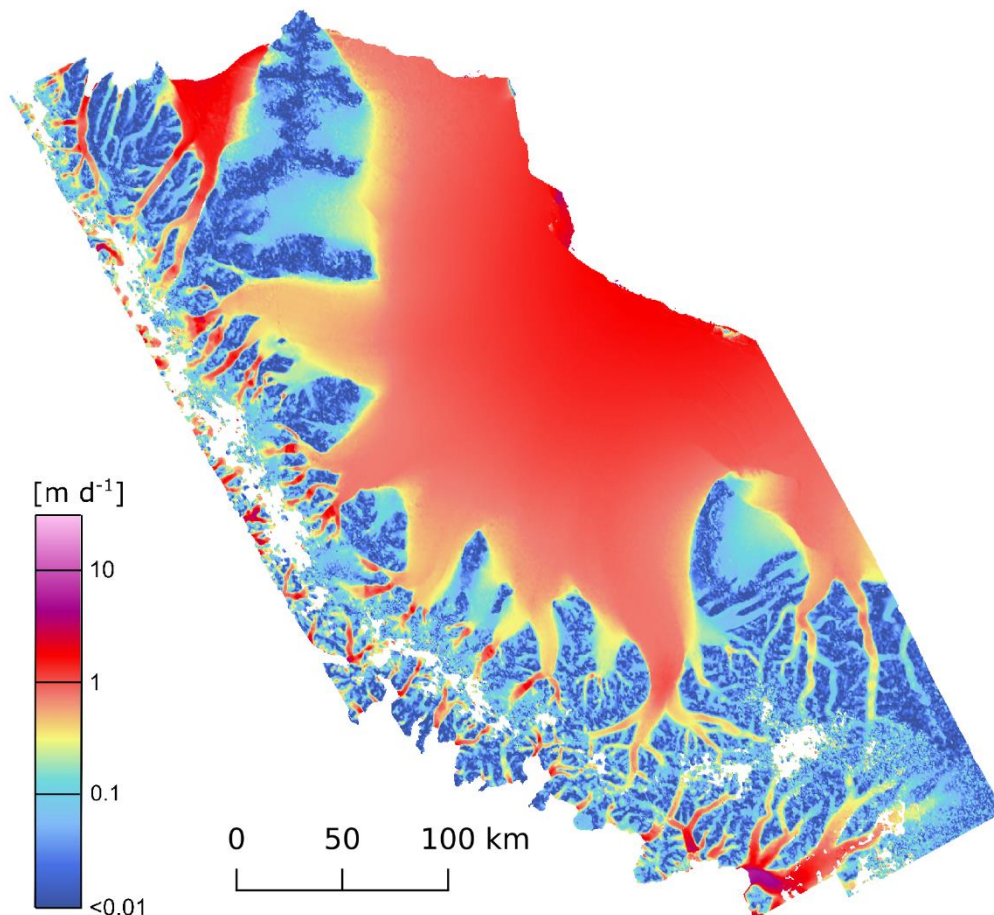


Figure 4.2: Sentinel-1 Ice Velocity averaged over a 6 month period: 2018/10/01-2019/03/31. The map is used as reference velocity map for the round robin exercise.

4.3 Round Robin Package & Steps

The Round Robin package was provided to all participants via FTP and included the following datasets:

- Sentinel-1A & -1B SLC data IW swath mode covering the region of interest (Larsen C) and period of interest (Jan/Feb 2019): Track 038, 3 slices, 6 dates (5 repeat intervals) acquired from ESA SciHub (Figure 4.3).
- Precise Orbit Ephemerides (AUX_POEORB) for the selected dates acquired from <https://qc.sentinel1.eo.esa.int/>
- DEM; Based on the REMA DEM Release 1.1 200m filled mosaic (Howat et al., 2019), corrected for geoid undulation using the Goco05s Geoid (Pail et al., 2016).



Name
S1A_IW_SLC_1SSH_20190115T080206_20190115T080233_025485_02D330_47B7.zip
S1A_IW_SLC_1SSH_20190115T080231_20190115T080258_025485_02D330_C11F.zip
S1A_IW_SLC_1SSH_20190115T080255_20190115T080322_025485_02D330_02C4.zip
S1A_IW_SLC_1SSH_20190127T080205_20190127T080232_025660_02D998_7690.zip
S1A_IW_SLC_1SSH_20190127T080230_20190127T080257_025660_02D998_74D5.zip
S1A_IW_SLC_1SSH_20190127T080255_20190127T080322_025660_02D998_BE89.zip
S1A_IW_SLC_1SSH_20190208T080205_20190208T080232_025835_02DFE0_F335.zip
S1A_IW_SLC_1SSH_20190208T080230_20190208T080257_025835_02DFE0_AE1F.zip
S1A_IW_SLC_1SSH_20190208T080254_20190208T080321_025835_02DFE0_823A.zip
S1B_IW_SLC_1SSH_20190109T080124_20190109T080151_014414_01AD4D_063E.zip
S1B_IW_SLC_1SSH_20190109T080149_20190109T080216_014414_01AD4D_70F0.zip
S1B_IW_SLC_1SSH_20190109T080214_20190109T080241_014414_01AD4D_DC39....
S1B_IW_SLC_1SSH_20190121T080214_20190121T080240_014589_01B2E6_0DEC.zip
S1B_IW_SLC_1SSH_20190121T080238_20190121T080305_014589_01B2E6_9529.zip
S1B_IW_SLC_1SSH_20190121T080303_20190121T080331_014589_01B2E6_4E8F.zip
S1B_IW_SLC_1SSH_20190202T080124_20190202T080151_014764_01B890_F9EE.zip
S1B_IW_SLC_1SSH_20190202T080148_20190202T080215_014764_01B890_A19D.zip
S1B_IW_SLC_1SSH_20190202T080213_20190202T080240_014764_01B890_67A5.zip

Figure 4.3: Input SLC data and coverage (Track 38)

The participants were asked to download RR package from ftp site and to generate IV maps in the projection of the DEM at 200m resolution (5 maps – 6-day repeats, easting & northing components). Requested was to provide upload back IV maps with and without tidal correction applied for the following 5 repeat intervals:

1. 20190109 - 20190115
2. 20190115 - 20190121
3. 20190121 - 20190127
4. 20190127 - 20190202
5. 20190202 – 20190208

Along with the input data sets a feedback form was provided to each participant for detailing information on pre-processing, offset estimation, post-processing, tidal/atmospheric correction, transition to grounded ice, timing, computational cost etc.). The completed response forms are provided in Section 4.6.

4.4 Results

4.4.1 Tidal Correction Methods

Table 4.1 summarizes the main characteristics and differences in the approaches for retrieval of tidal corrected ice velocity by the RR participants as detailed in the RR feedback forms (Section 4.6). The general approach for coregistration and offset estimation is similar, but there are differences in matching window size, posting, and post-processing (outlier removal/gap filling, calibration etc.), which are not listed in the table. For tidal correction all participants utilized the CATS2008 tide model developed by Padman et al. (2002, 2008) and provided on a 4km grid by the U.S. Antarctic Program Data Center (USAP-DC)(Howard et al., 2019). The tide estimates are extracted for each pixel for the acquisition timestamps of the master/slave scenes including all tidal constituents included in the model (M2, S2, N2, K2, K1, O1, P1, Q1, Mf, Mm). The tides are corrected for atmospheric pressure at these time stamps and are scaled by a factor of 0.95-1.00 cm/hPa. The modelled vertical displacement is projected to SAR geometry for correcting the range offsets. The main differences w.r.t. tidal correction methodology are the atmospheric model used and the handling of the transition at the grounding line. For atmospheric correction both ENVEO and DLR have used the NCEP/NCAR Reanalysis data set provided by NOAA (4x daily, 2.5°), DTU have used ERA5 surface pressure provided by ECMWF through the Copernicus Climate Data Store (CDS)(hourly, 0.25°). The transition zone at the grounding line is treated differently by all participants. Both ENVEO and DTU applied a transition zone at the grounding line (MEaSURES, Rignot et al., 2016). ENVEO applied an elastic beam model (see Section 3.3.1) while DTU uses a transition zone of

2km from the grounding line over which the tidal/pressure correction is increased linearly from 0 to 100% at the 2km line. DLR did not apply a transition zone at the grounding line and the correction is applied for each pixel within the CATs2008 domain. Processing time of the tidal correction is in general negligible relative to the offset estimation.

Table 4.1: Main characteristics for tidal corrected ice velocity by RR participants

	ENVEO	DTU	DLR
Offset Estimation	Incoherent cross-correlation	Incoherent cross-correlation	Incoherent cross-correlation
Tide Model	CATS2008	CATS2008	CATS2008
Atmospheric model	NCEP/NCAR 4-times daily 2.5° x 2.5° global grids Scaling : 1cm/hPa	ERA5 pressure levels Hourly 0.25° x 0.25° global grids Scaling : 1cm/hPa	NCEP/NCAR 4-times daily 2.5° x 2.5° global grids Scaling : 0.95 cm/hPa
Transition	Measures GLL Elastic beam model, ~5km	Measures GLL Linear transition, 2km	CATS2008 domain No transition
Correction geometry	SAR, 40x20 px	SAR, 40x10 px	SAR, 64x64 px

4.4.2 Participant Intercomparison

This section shows the results of the intercomparison of the ice velocity maps provided by the RR participants. All provided maps (Figure 4.4), both uncorrected and tidally corrected, were compared on a pixel-by-pixel level for the easting (E) and northing (N) velocity components. Presented here are the statistical (mean, RMSE) results of the intercomparisons (Table 4.2). For graphical representation we provide histograms, spatial difference maps and scatterplots of the easting component residuals for selected dates (Figure 4.5, Figure 4.6). The easting component corresponds approximately to the range direction and is most affected by tide.

Table 4.2: Statistics of participant intercomparison. For the statistics only common data points are included and differences that exceed 1 m/d are excluded. Values are in m/d.

	Date	Tide Corrected				Uncorrected				Pixels (x10 ⁶)
		Mean E	RMS E	Mean N	RMS N	Mean E	RMS E	Mean N	RMS N	
ENVEO DTU	20190109-20190115	0.00	0.07	0.00	0.11	-0.01	0.07	-0.01	0.11	1.8
	20190115-20190121	-0.01	0.09	0.06	0.16	-0.01	0.09	0.06	0.16	1.5
	20190121-20190127	-0.05	0.08	0.05	0.10	-0.05	0.08	0.05	0.10	1.8
	20190127-20190202	-0.01	0.06	0.04	0.09	-0.01	0.05	0.04	0.09	1.6
	20190202-20190208	-0.03	0.07	0.05	0.10	-0.03	0.06	0.05	0.10	1.6
ENVEO DLR	20190109-20190115	0.07	0.17	0.10	0.20	-0.01	0.13	0.05	0.18	1.4
	20190115-20190121	-0.16	0.24	-0.12	0.22	-0.01	0.13	-0.04	0.18	1.3
	20190121-20190127	0.15	0.24	0.14	0.21	-0.02	0.12	-0.05	0.14	1.6
	20190127-20190202	-0.14	0.19	-0.13	0.19	-0.01	0.11	-0.07	0.15	1.5
	20190202-20190208	0.02	0.10	0.07	0.14	0.01	0.11	0.06	0.15	1.3

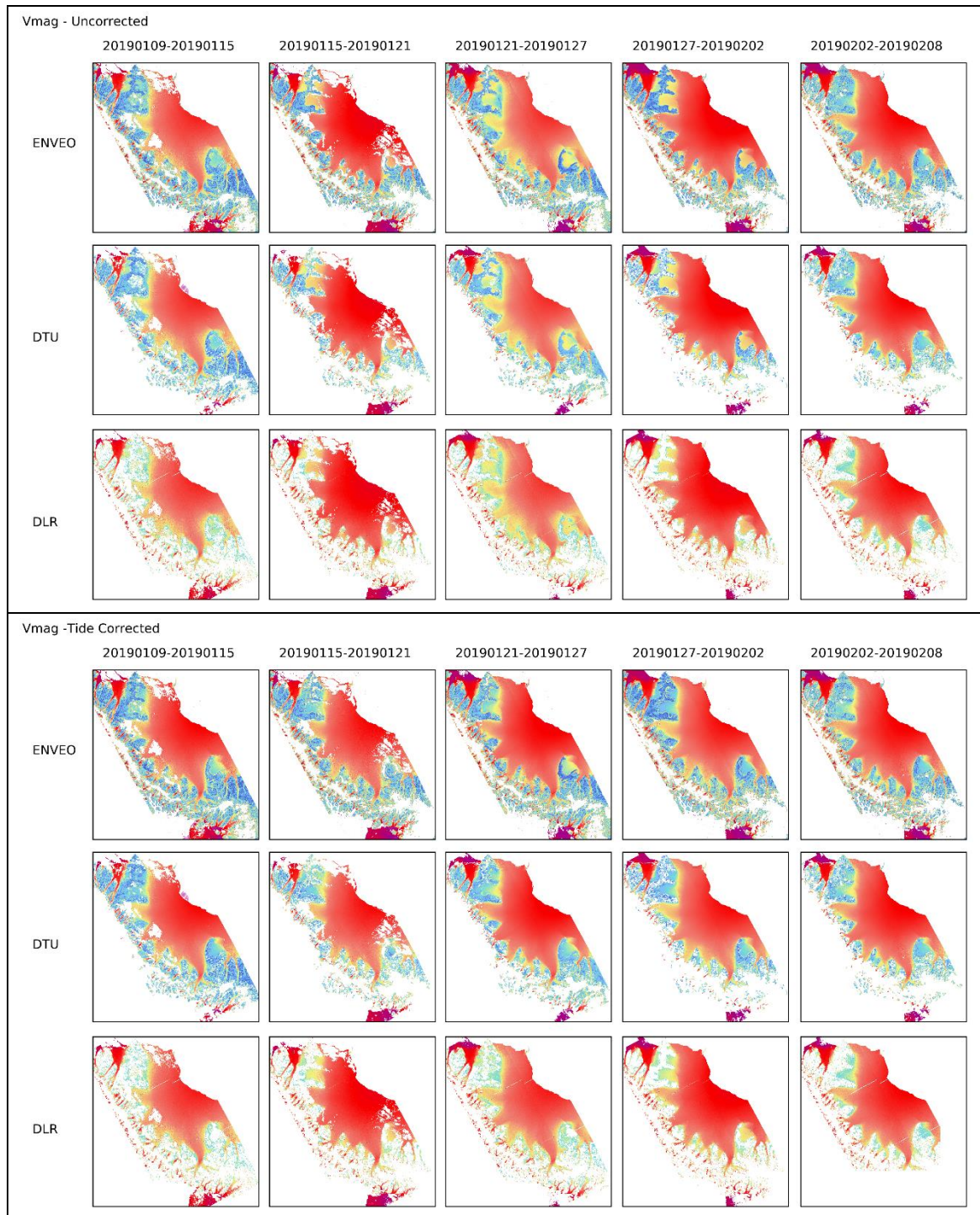
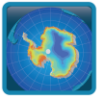


Figure 4.4: Overview of the velocity maps provided by the RR participants (depicted is the velocity magnitude). Top panel: uncorrected, Bottom panel: tidally corrected.

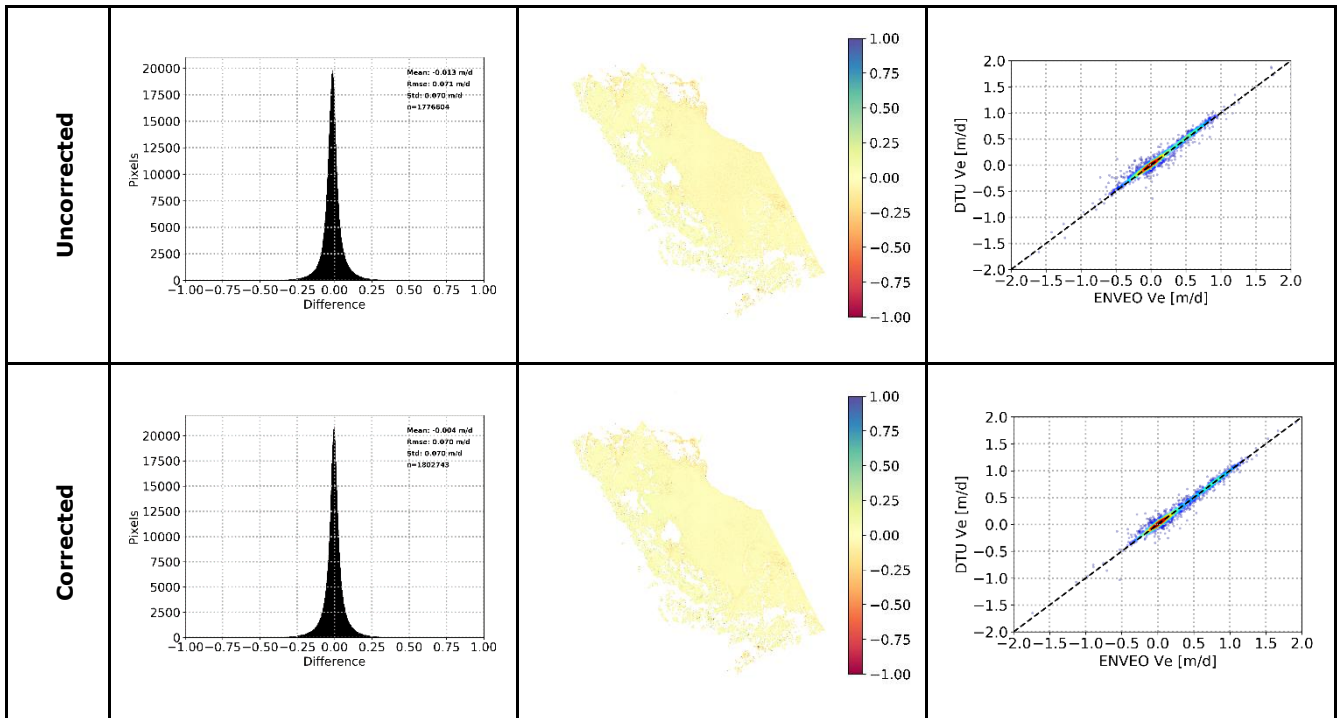


Figure 4.5: ENVEO-DTU comparison for 20190109-20190115. Displayed are histograms of residuals of the easting velocity component (left; values in m/d), difference maps (middle; values in m/d) and scatterplots with color-coding (blue-red) according to data density, the dashed line is the identity line (right).

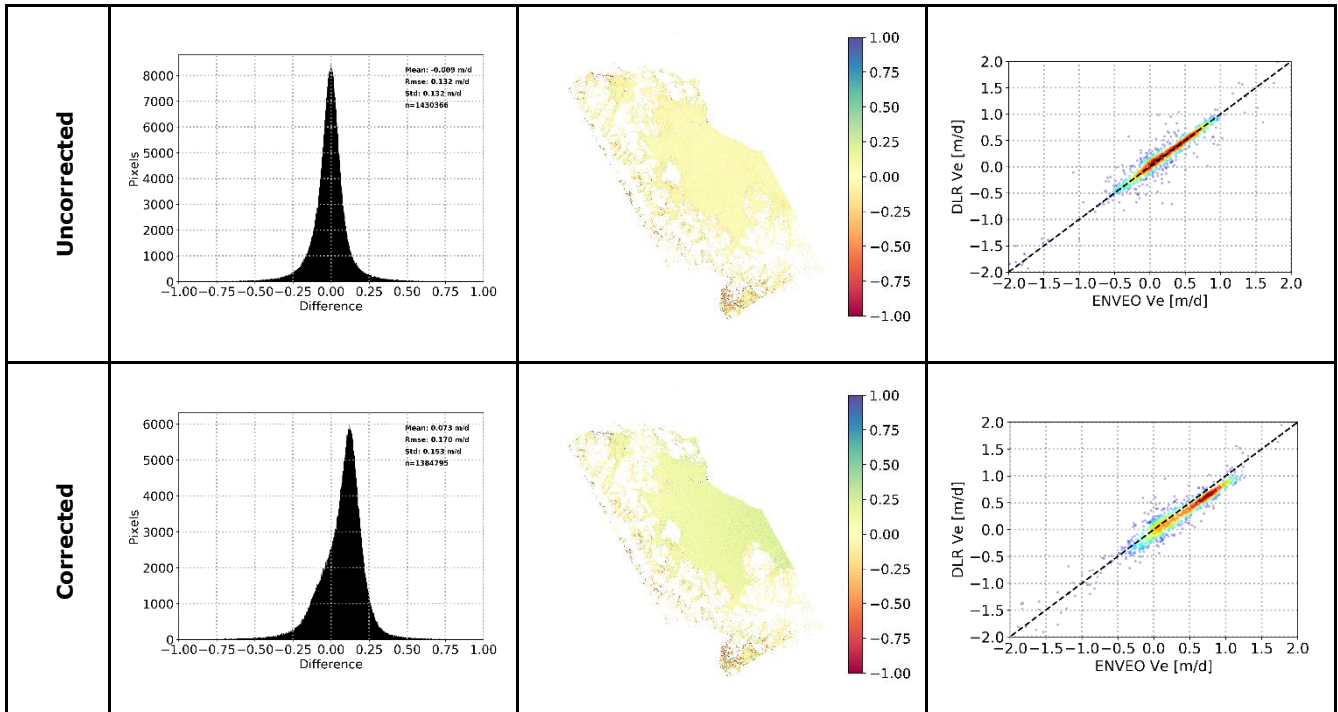


Figure 4.6: ENVEO-DLR comparison for 20190109-20190115. Displayed are histograms of residuals of the easting velocity component (left; values in m/d), difference maps (middle; values in m/d) and scatterplots with color-coding (blue-red) according to data density, the dashed line is the identity line (right).

The results of the participant intercomparison show a good agreement between ENVEO and DTU before and after tide correction with mean differences in both V_e and V_n of 0-5 cm/d and RMSE \sim 10 cm/d. The small differences between uncorrected and corrected data indicate that these can be largely ascribed to processing settings and post-processing (e.g. outlier removal). There is also a good agreement between the ENVEO and DLR data sets before tide correction with mean differences between $V_e < 2$ cm/d (RMS \sim 12 cm/d) and V_n 4-7 cm/d (RMS 14-18 cm/d), but mean differences and spreading become larger after tide correction.

4.4.3 Reference Intercomparison

This section shows the results of the intercomparison of the ice velocity maps provided by the RR participants with the reference 6-month averaged velocity map (Figure 4.2). As in previous section the provided maps (Figure 4.4), both uncorrected and tidally corrected, were compared on a pixel-by-pixel level for the easting and northing velocity components. Presented here are the statistical results (mean, RMSE) of the intercomparisons (Table 4.3). For graphical representation we provide histograms and spatial difference maps of the easting component residuals for all processed date pairs by the RR participants (Figure 4.7, Figure 4.8 and Figure 4.9).

The results clearly illustrate the efficacy of the tide corrections for all participants, with the ENVEO and DTU approaches in close agreement and best performing. The residuals of the uncorrected ice velocity map w.r.t. the reference map have a clear bi-modal distribution, with one peak corresponding to grounded ice and the other to the floating ice. This is also clearly observed in the difference plots, showing nicely the distinction between the floating sections of Larsen C and SCAR Inlet ice shelves and grounded ice. In the tide corrected data, the bi-modal distribution is no longer present, and the difference maps show good agreement with the longer-term averaged ice velocity. The mean differences of the velocity (easting and northing components) are in most cases strongly reduced from 10/20+ cm/day to only 1-5 cm/day with an RMSE in the order of 10 cm/d.

Table 4.3: Statistics of residuals with the reference ice velocity map. Only common data points are included and differences that exceed 1 m/d are excluded.

	Date	Tide Corrected				Uncorrected				Pixels ($\times 10^6$)
		Mean E	RMS E	Mean N	RMS N	Mean E	RMS E	Mean N	RMS N	
ENVEO	20190109-20190115	-0.01	0.11	-0.02	0.15	-0.11	0.19	-0.07	0.18	2.1
	20190115-20190121	-0.01	0.12	0.01	0.17	0.19	0.28	0.11	0.22	1.9
	20190121-20190127	0.04	0.12	0.04	0.14	-0.19	0.29	-0.09	0.19	2.1
	20190127-20190202	-0.02	0.11	-0.02	0.14	0.14	0.22	0.07	0.16	2.0
	20190202-20190208	0.03	0.12	0.02	0.14	0.00	0.11	0.01	0.14	2.0
DTU	20190109-20190115	-0.01	0.08	-0.02	0.12	-0.12	0.17	-0.07	0.16	1.8
	20190115-20190121	-0.01	0.09	-0.05	0.16	0.25	0.32	0.09	0.18	1.4
	20190121-20190127	0.10	0.12	-0.01	0.10	-0.18	0.27	-0.16	0.19	1.8
	20190127-20190202	-0.02	0.06	-0.06	0.10	0.20	0.24	0.06	0.11	1.5
	20190202-20190208	0.07	0.09	-0.03	0.11	0.03	0.07	-0.05	0.11	1.6
DLR	20190109-20190115	-0.08	0.17	-0.13	0.20	-0.15	0.22	-0.16	0.23	1.4
	20190115-20190121	0.15	0.22	0.13	0.22	0.28	0.34	0.19	0.28	1.3
	20190121-20190127	-0.09	0.19	-0.10	0.17	-0.23	0.32	-0.18	0.24	1.5
	20190127-20190202	0.11	0.17	0.11	0.17	0.21	0.27	0.17	0.22	1.4
	20190202-20190208	0.02	0.11	-0.04	0.14	0.00	0.12	-0.05	0.15	1.3

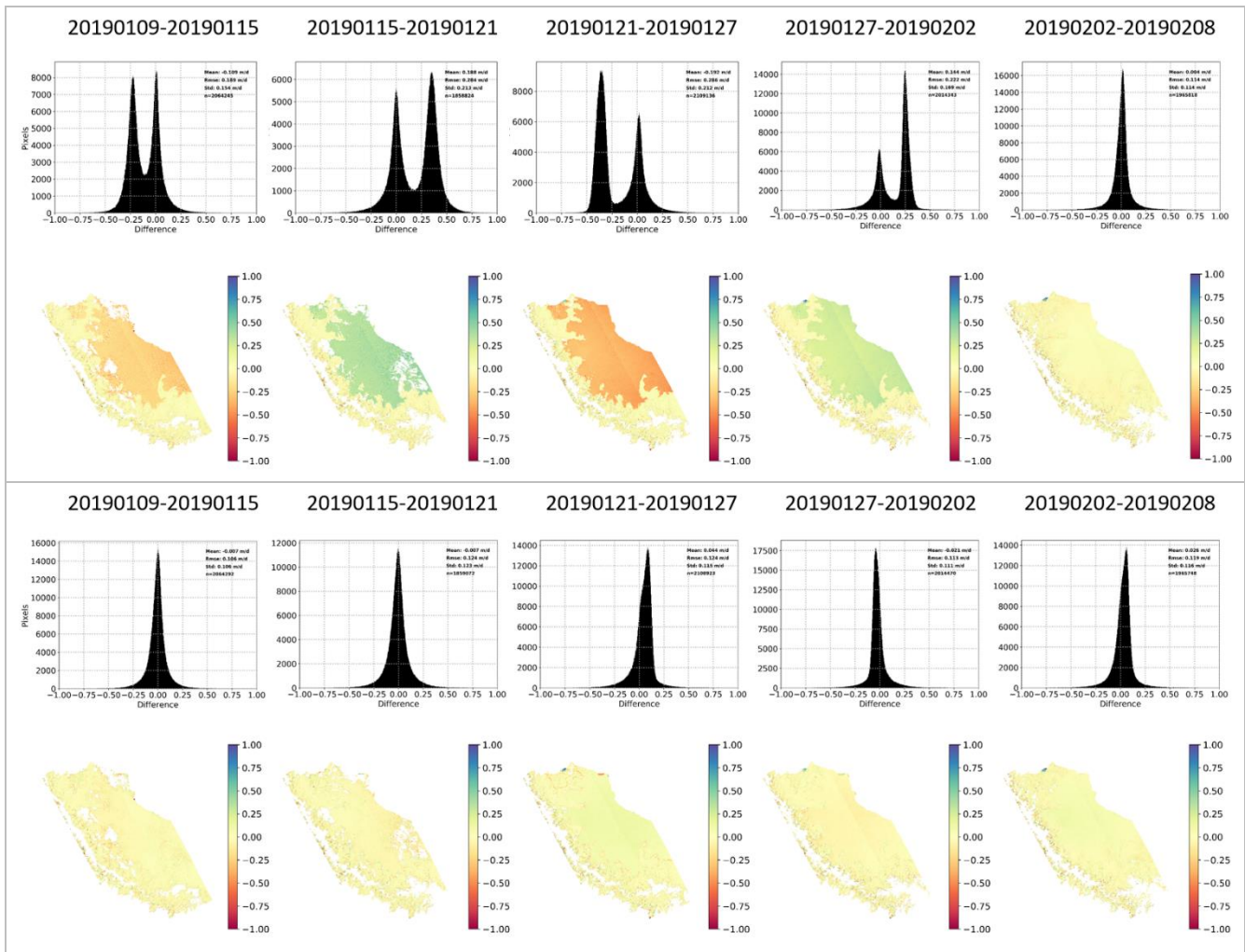


Figure 4.7: Histograms and difference maps for the reference map intercomparison for ENVEO. Displayed are the residuals of the easting velocity component. Top: uncorrected, Bottom: corrected. Values in m/d.

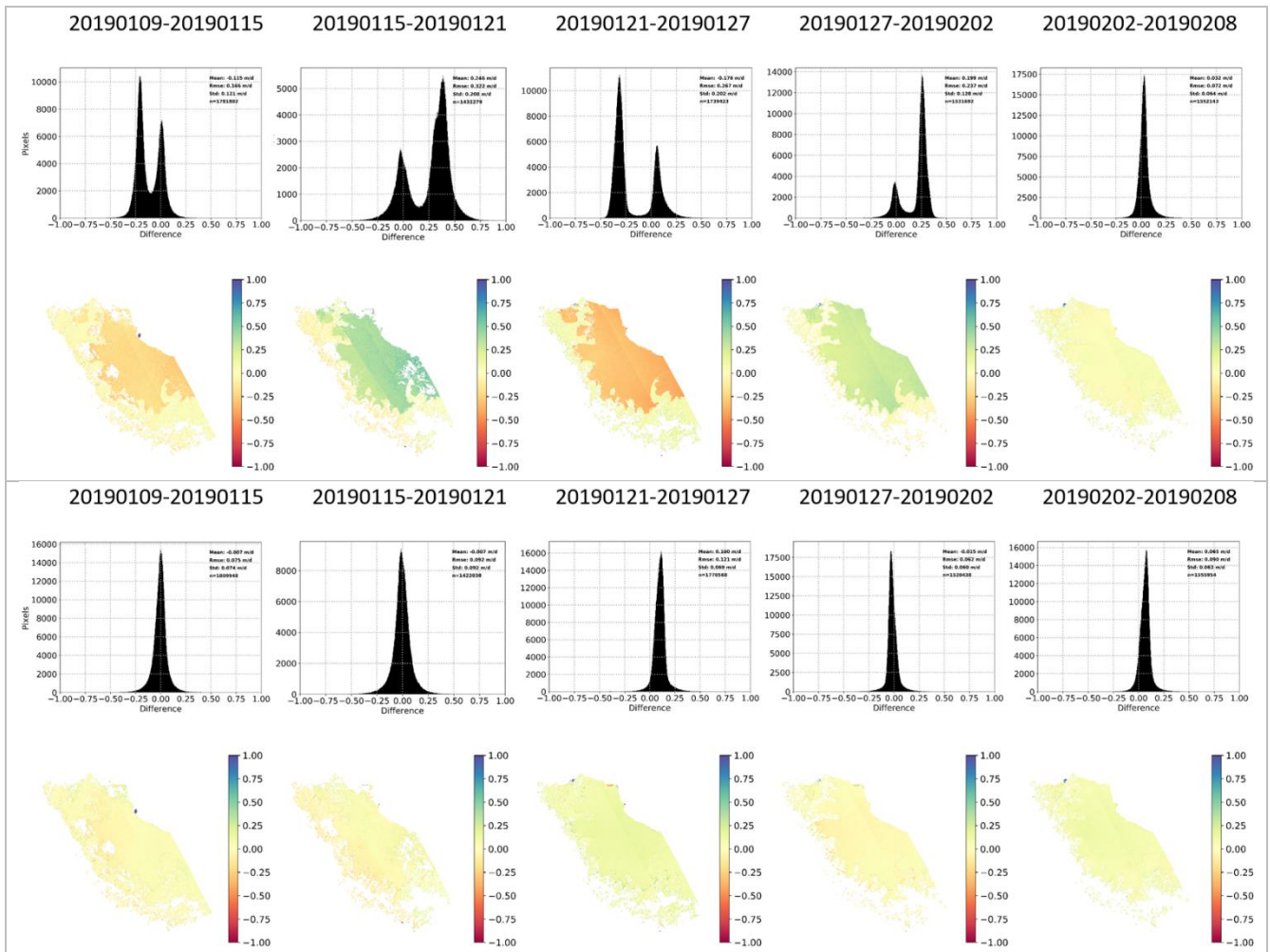


Figure 4.8: Histograms and difference maps for the reference map intercomparison for DTU. Displayed are the residuals of the easting velocity component. Top: uncorrected, Bottom: corrected. Values in m/d.

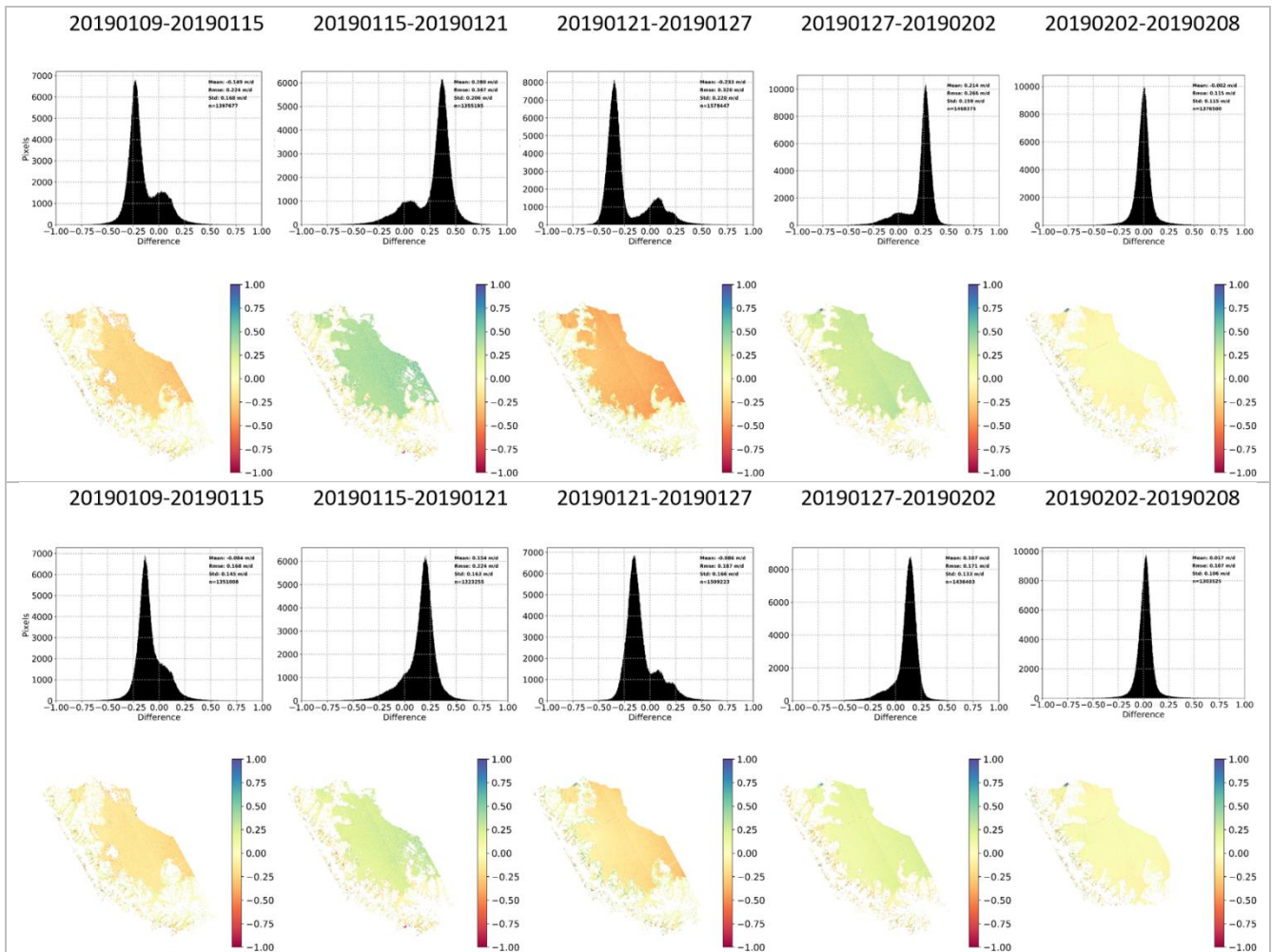


Figure 4.9: Histograms and difference maps for the reference map intercomparison for DLR. Displayed are the residuals of the easting velocity component. Top: uncorrected, Bottom: corrected. Values in m/d.

4.4.4 Tide Model Intercomparison

The latest tide model in the TPXO family (Egbert and Erofeeva, 2002) is TPXO9-atlas. This is a global ocean tide model with updated bathymetry at a resolution of 1/6 degree globally and nested local solutions at coastal areas with a 1/30-degree resolution, including Antarctica. Satellite altimetry data was used to best-fit the Laplace Tidal Equations in the least squares sense and to obtain the model (data access: <https://www.tpxo.net/global/tpxo9-atlas>). For the RR we tested the model using the RR data set and reference velocity map and compared the outcomes with the CATS2008 model results.

In general, we found that the results agree quite well, but for some periods there is a notable difference. Figure 4.10 illustrates an example for the period 20190121-20190127, showing the difference between both models based on an intercomparison with the reference ice velocity map (Figure 4.2). Displayed are, for both models, histograms of the residuals of the easting velocity component and scatterplots. Based on this, the TPXO9-atlas shows a clear improvement: the mean offset is reduced from 4 cm/d to 1 cm/d and the scatter plot shows a closer agreement, especially at higher velocities. However, looking into closer detail at the difference maps reveals an obvious artefact near the grounding line of SCAR Inlet Ice Shelf (formerly a section of Larsen B) for the TPXO9-atlas tide corrected map that is not present in the CATS2008 tide corrected map (Figure 4.11). The artefact appears to be related to the coarser land mask used for the TPXO9-atlas model (Figure 4.12), resulting in sections of the ice shelf not corrected for tides. In general, we found the land mask of CATS2008 to be in closer agreement with the grounding line.

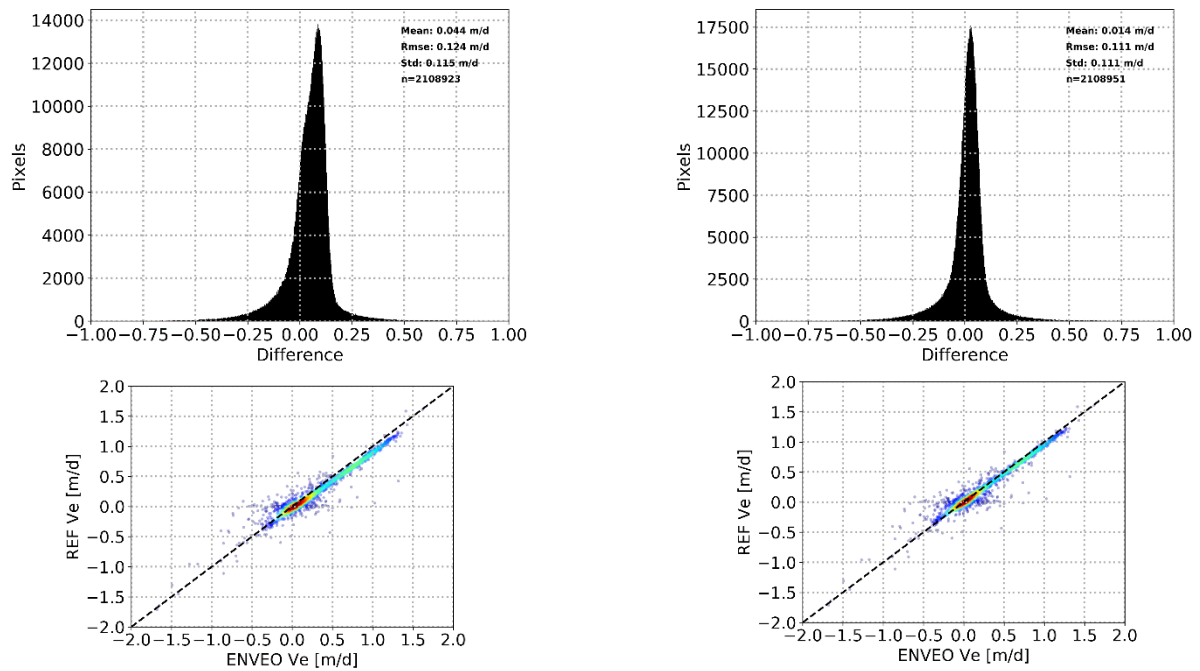


Figure 4.10: Histograms of the residuals of the easting velocity component (top) and scatterplots (bottom) for CATS208 (left) and TPX09-atlas (right) for 20190121-20190127. The scatter plots are color-coded (blue-red) according to data density, the dashed line is the identity line.

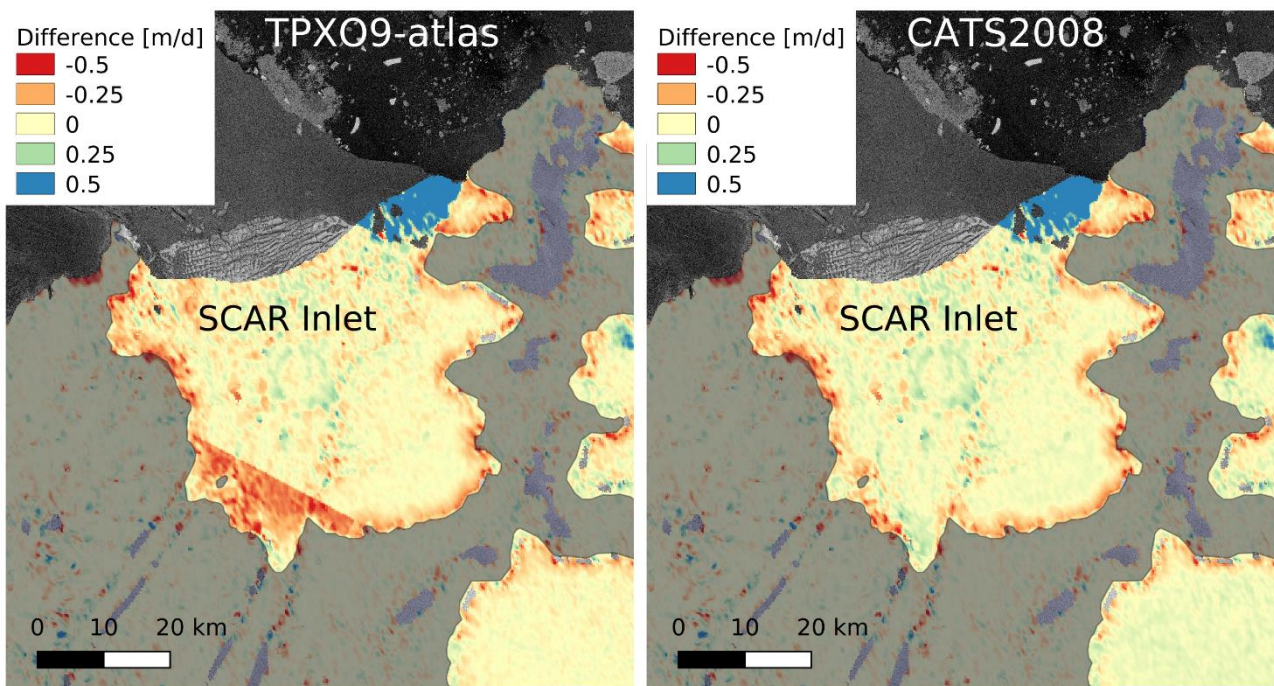


Figure 4.11: Difference between tide corrected velocity and reference velocity on SCAR Inlet Ice Shelf for 20190121-20190127. Left: TPX09-atlas, Right: CATS208. Background: Sentinel-1 amplitude image acquired on 20190109.

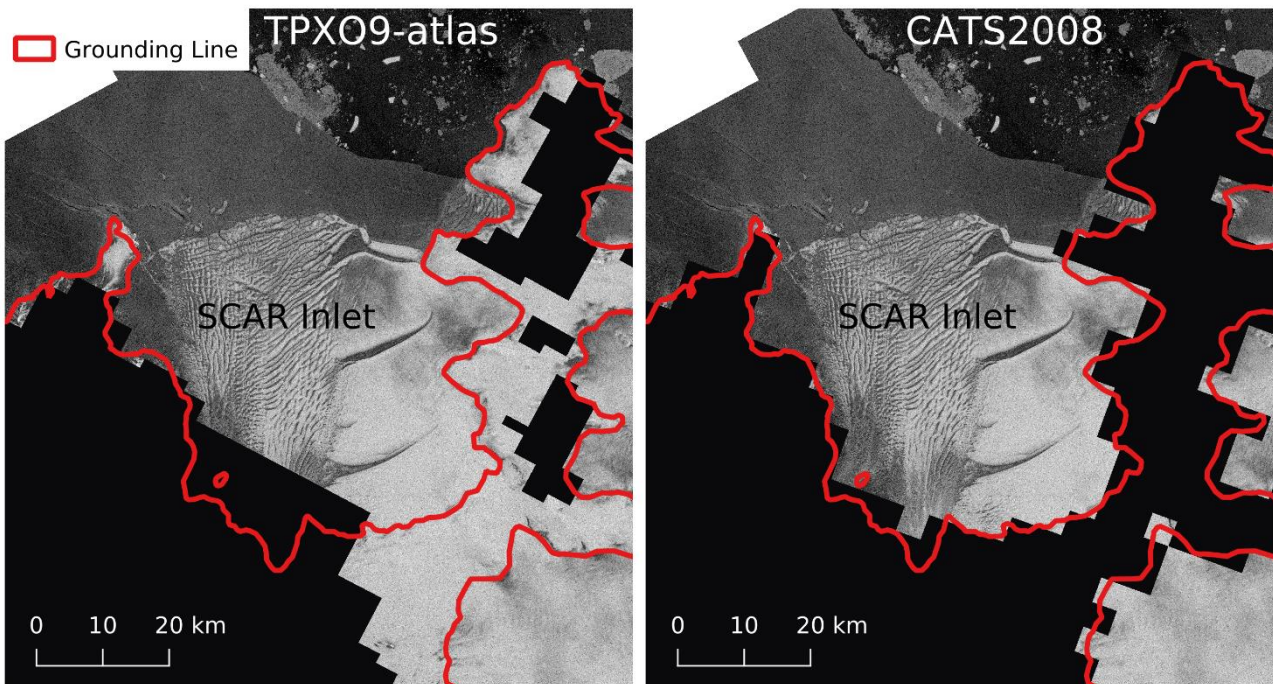


Figure 4.12: Land mask for TPX09-atlas (left) and CATS2008 (right) on SCAR Inlet Ice Shelf. The red line is the MEaSUREs grounding line (Rignot et al., 2016). Background: Sentinel-1 amplitude image acquired on 20190109.

4.4.5 Surface Pressure Reanalysis Dataset Comparison

We tested two different surface pressure reanalysis datasets:

1. NCEP/NCAR Reanalysis 1: NOAA Earth System Research Laboratory provides daily global reanalysis datasets of climate variables. The surface pressure reanalysis subset comprises four global surface pressure maps (0.995 sigma level) with a spatial coverage of 2.5-degree latitude x 2.5-degree longitude grid. Reanalysis timestamps are 0Z, 6Z, 12Z, and 18Z (Kalnay *et al.*, 1996).
2. ERA5 surface pressure reanalysis: The surface pressure is hourly provided in Pascal on a global grid with a spatial resolution of 0.25°x0.25° (C3S, 2017).

To extract the surface pressure the acquisition time stamps are rounded to the nearest available time stamp. For NCEP the available temporal layers are 00:00Z, 06:00Z, 12:00Z and 18:00Z whereas for ERA5 hourly data is available. Figure 4.13 shows the difference in surface pressure. In the left panel the difference between NCEP data from 2 Feb. 2019 at 06:00Z and 8 Feb. 2019 at 06:00Z. Due to the higher temporal resolution ERA5 maps were derived for 2 Feb. 2019 at 08:00Z and 8 Feb. 2019 at 08:00Z. Both difference maps capture the pressure difference of ~1800Pa on the west coast of the Antarctic Peninsula. ERA5 better resolves the smaller scale differences over Larsen A and B, improving the IBE correction. Both data sets are freely available. NCEP has latency of one day, ERA5 is available within 5 days of real time. Table 4.4 shows the main characteristics of NCEP and ERA5 surface pressure reanalysis.

Table 4.4: Characteristics of NCEP and ERA5 surface pressure reanalysis.

	NCEP	ERA5
Spatial resolution	2.5°x2.5°	0.25°x0.25°
Temporal resolution	4-times daily	hourly
File type	NetCDF	NetCDF
Data volume/Year	~23.4 MB	~2.6GB

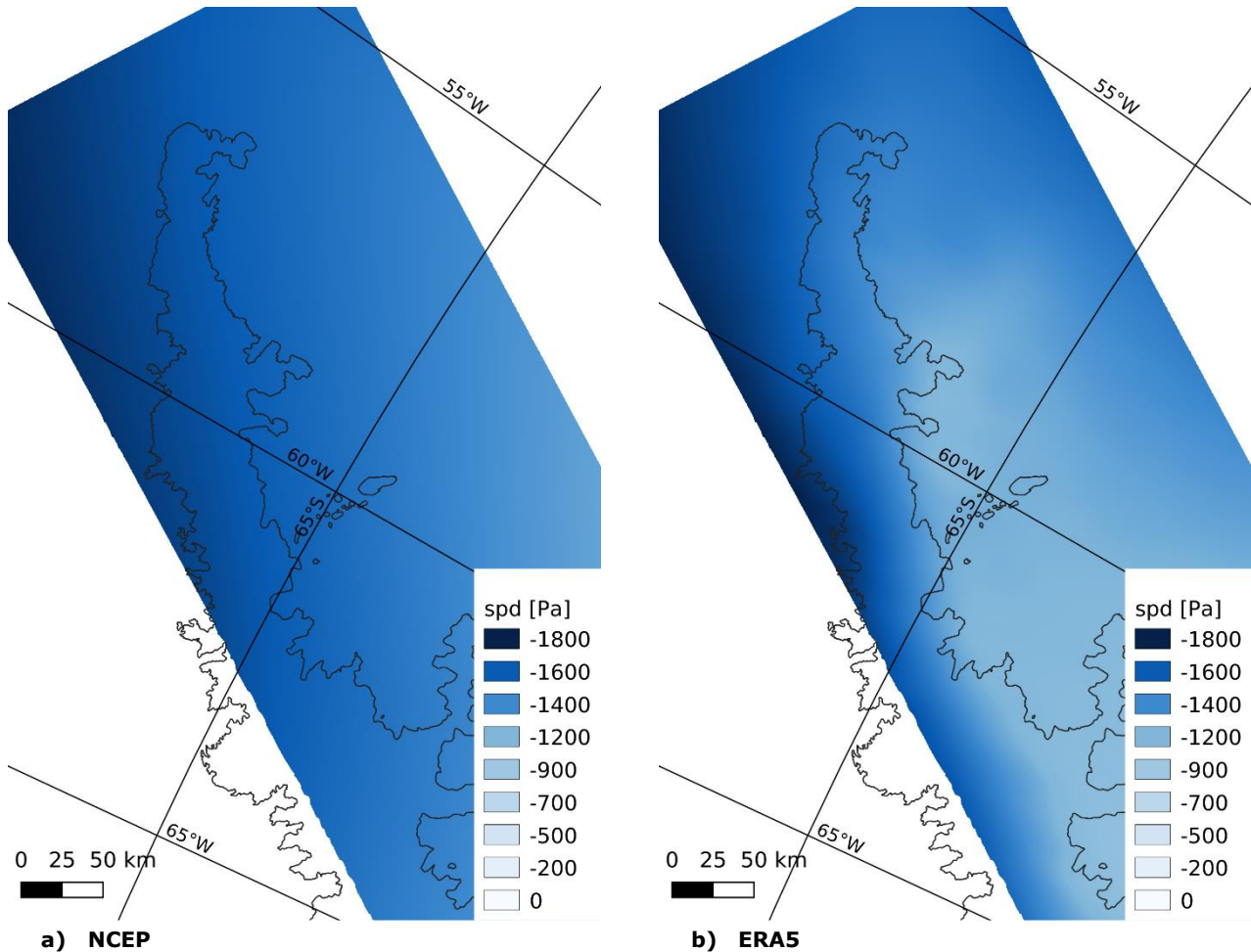
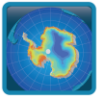


Figure 4.13: Comparison of NCEP and ERA5 surface pressure difference (spd) maps covering Antarctic Peninsula. The layer with the closest timestamp to the acquisition date are extracted and subtracted from each other. NCEP with the coarser grid smoothens the smaller scale pressure differences at Larsen A and B which are still resolved by ERA5.

4.5 Summary & Conclusions

This appendix gives an overview of the activities and main outcome of the RR for tide correction of velocity on ice shelves. Contributions by experts in the field of ice velocity retrieval have made the RR a valuable exercise for determining and selecting the most suitable approach and models. Based on the outcome the general approach outlined in Chapter 3 is selected and implemented. Figure 4.14 serves as illustration of the improvement achieved by implementing the tide correction. Remaining deviations can form the basis for further improvement of existing tide models. The CATS2008 tide model currently implemented by all RR participants is the preferred model at present. The TPX09-atlas model is not deemed ideal for tide correction until Antarctic bathymetry is coordinated with MEaSUREs Antarctic Boundaries data. Additionally, we have been made aware that licensing is required for TPXO derived digital products. For atmospheric pressure correction, although differences are minor, the ERA5 reanalysis pressure fields will be used: the high spatial and temporal resolution of this data set is of benefit for the correction of the inverse barometer effect on ice shelves.

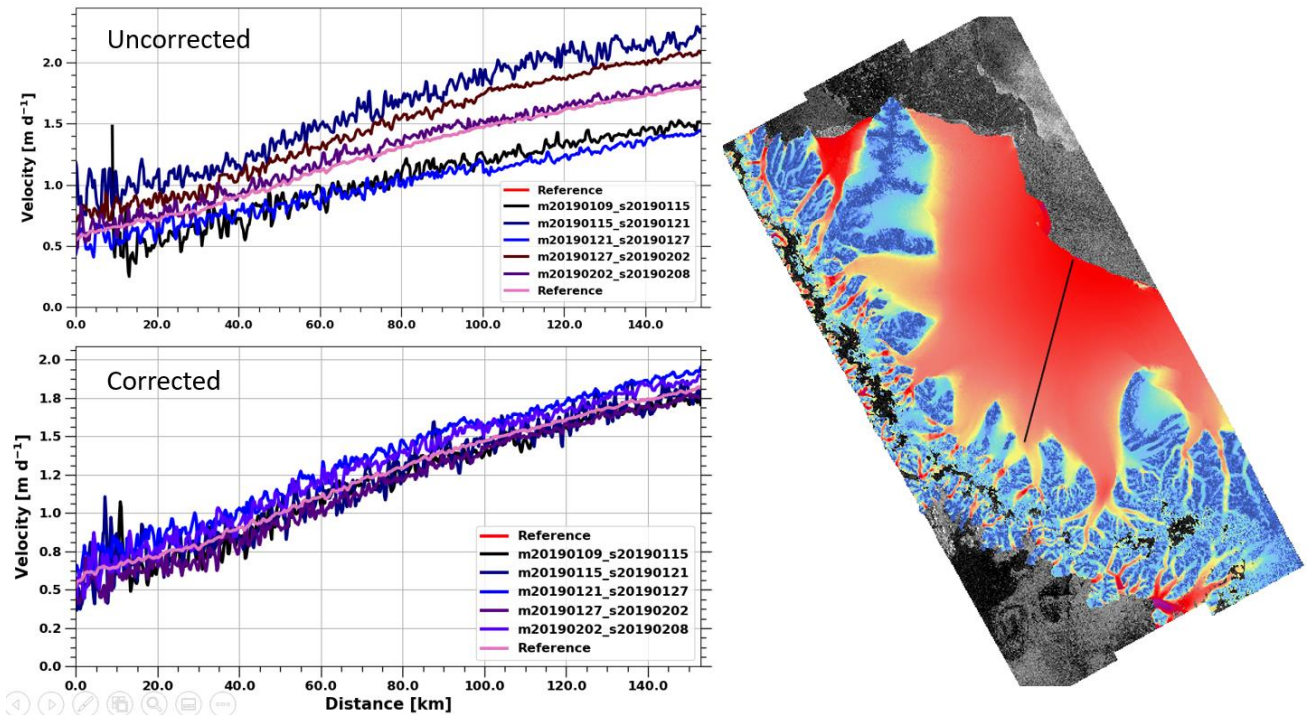
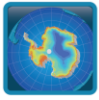


Figure 4.14: Ice velocity (magnitude) along a profile before (top) and after (bottom) tide correction. Location of the profile is indicated on the velocity map (right).

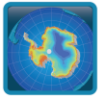
4.6 Feedback Forms

4.6.1 Enveo

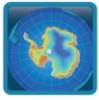
Antarctic IceSheets_CCI+ Round Robin: Ice Velocity on Ice Shelves (IVonIS) Feedback Form	
<u>Participant Information</u>	
Name	Jan Wuite, Markus Hetzenecker, Stefan Scheiblauer
Affiliation	ENVEO It
Address	Fürstenweg 176, 6020 Innsbruck, Austria
Email	jan.wuite@enveo.at, markus.hetzenecker@enveo.at, stefan.scheiblauer@enveo.at
<u>Software Specifications</u>	Specify which software(s) were used for data processing. If available, list papers, manuals etc containing the software specifications and documentation.
ENVEO SAR Software Package (ESP) Version 2.1; Python module pyTMD	
<u>Processing Specifications</u>	Please provide the following information - alternatively, you may cite a publication where this information is provided.



Co-registration	Master / Slave Coregistration applied	Yes
	Brief discription of the co- registration procedure (e.g. how was orbital data used and which refinement algorithm was applied: geometric, data matching, etc)	Precise orbits and DEM
Pre-Processing procedures:	Brief description of pre-processing routines (e.g. global co- registration procedures, resampling strategies, image enhancements, multi-looking, etc.)	None
Offset estimation	Method applied (e.g. CrossCorrel, Least Squares, etc)	Incoherent cross-correlation
	Matching window size	128x64 (range x azimuth)
	Search window size (if different)	same
	Search window posting	40 x 20 (range x azimuth)
	Oversampling factor (if applicable)	2
	Matching quality measure	correlation threshold: 0.05
	Describe the details of your image matching methods (e.g.	Constant window size on regular grid; number of iterative runs: 3; Geolocated shift vectors transformed to Projection of DEM.

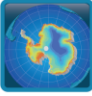


	variable or constant window sizes, correlation routines, etc.)	
Post-Processing procedures	Detailed description of all post-processing routines (incl. outlier culling, calibration, etc.):	Std Filter: 5x5; Smoothing Filter: 3x3; Gap Filling: 5x5, 1 st order planefit; Calibration against overall Sentinel-1 AIS map.
	Specific filters applied (e.g. box filter, ionosphere filter)	n/a
Tidal & Atmospheric Pressure Correction	Tidal model used (+version, resolution & source)	CATS2008, 4x4 km https://www.esr.org/polar_tide_models/Model_CATS2008a.html
	Atmospheric model used (+version, resolution & source)	NCEP Reanalysis (Surface pressure, 4-times daily), 2.5 degree latitude x 2.5 degree longitude global grid (144x73) http://www.esrl.noaa.gov/psd/data/gridded/data.ncep.reanalysis.html
	Detailed description of tidal correction-processing routines (include information on: Sampling (one point or grid?); Grid spacing of the used models (any oversampling applied?); Method to handle transition to grounded ice, Any specific parameter settings etc.)	Tides including all constituents are predicted for each point in the geolocation grid (lat/long in SAR geometry) for the acquisition timestamps of the master/slave scene. For the same time points the surface pressure is bilinearly interpolated within reanalysis dataset to the geolocation grid. The tidal difference is corrected for the IBE applying a scaling factor of -1 cm/hPa to the surface pressure difference. To ensure a smooth transition from grounded ice to floating ice a mask is used where the transition zone is modelled with an elastic beam. Mapping the corrected tidal displacement to SAR geometry and normalizing it with the time lag between the acquisitions gives the correction term for the ice velocity.
Overall Processing Info	Processing Duration (CPU Time)	~35 minutes / stripe pair (3 slices): feature tracking: 30 mins; filter/geocoding/calibration/tide correction: 5 mins



4.6.2 DLR

Antarctic IceSheets_CCI+ Round Robin: Ice Velocity on Ice Shelves (IVonIS)		
Feedback Form		
<u>Participant Information</u>		
Name	Erling Johnson, Lukas Krieger, Dana Floricioiu	
Affiliation	DLR	
Address	Münchener Str. 20, 82234 Wessling, Germany	
Email	erling.johnson@dlr.de , lukas.krieger@dlr.de , dana.floricioiu@dlr.de	
<u>Software Specifications</u> Specify which software(s) were used for data processing. If available, list papers, manuals etc containing the software specifications and documentation.		
IWAP - Interferometric Wide Swath Processor DLR, CATS tide model, NCEP Reanalysis (Air Pressure)		
<u>Processing Specifications</u> Please provide the following information - alternatively, you may cite a publication where this information is provided.		
Co-registration	Master / Slave Coregistration applied	Y
	Brief discription of the co-registration procedure (e.g. how was orbital data used and which refinement algorithm was applied: geometric, data matching, etc)	Refined Orbits are applied to the Master and Slave, then a coarse co-registration is performed.
Pre-Processing procedures:	Brief description of pre-processing routines (e.g. global co-registration procedures, resampling strategies, image enhancements, multi-looking, etc.)	The Master and Slave are Oversampled per burst and then mosaicked together per swath. At this point the possibility to multi-look is available but not applied in this case.
Offset estimation	Method applied (e.g. CrossCorrel, Least Squares, etc)	CrossCorrelation, Fourier Domain (Matching window = Search window)
	Matching window size	256px x 256px
	Search window size (if different)	[Fill Text here]
	Search window posting	64px x 64px
	Oversampling factor (if applicable)	2x2
	Matching quality measure	Correlation Coefficient

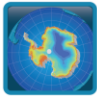
 antarctic ice sheet cci	Antarctica_Ice_Sheet_cci+ Algorithm Theoretical Basis Document (ATBD) for AIS CCI+ Phase 1	Reference: ST-UL-ESA-AISCCI+-ATBD-001 Version : 1.0 page Date : 9 March 2020 45/48
--	--	--

	Describe the details of your image matching methods (e.g. variable or constant window sizes, correlation routines, etc.)	Correlation performed in the Fourier domain with constant window size and posting, Resulting pixel positions in Master and Slave geolocated with respective orbit parameters and REMA DEM. Geolocated shift vectors transformed to Projection of REMA DEM epsg:3031.
Post-Processing procedures	Detailed description of all post-processing routines (incl. outlier culling, calibration, etc.):	Outlier removal according to Lüttig, Christine, Niklas Neckel, and Angelika Humbert. "A combined approach for filtering ice surface velocity fields derived from remote sensing methods." Remote Sensing 9.10 (2017): 1062.
	Specific filters applied (e.g. box filter, ionosphere filter)	[Fill Text here]
Tidal & Atmospheric Pressure Correction	Tidal model used (+version, resolution & source)	CATS2008a_opt from https://www.esr.org/polar_tide_models/Model_CATS2008a.html
	Atmospheric model used (+version, resolution & source)	NCEP Reanalysis (Air Pressure) http://www.esrl.noaa.gov/psd/data/gridded/data.ncep.reanalysis.html
	Detailed description of tidal correction-processing routines (include information on: Sampling (one point or grid?); Grid spacing of the used models (any oversampling applied?); Method to handle transition to grounded ice, Any specific parameter settings etc.)	Tide estimates are extracted for each pixel of the coregistration map (In radar coordinates) for two time points (Slave/Master). Tides are corrected for atmospheric pressure at these time points with a factor of -0.95 cm/hPa . The tidal difference is converted with a linearly interpolated incidence angle (near/far range) to a range shift in meters. The resulting offset in emters is converted to a pixel offset with the original SLC pixel spacing and removed from the coregistration range shifts. Processing continues as usual. This approach applies a tidel predication to all points of the velocity map that have valid tidal predictions in the CATS2008a_opt model.
Overall Processing Info	Processing Duration (CPU Time)	1h 30 min per Swath

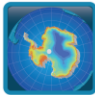
4.6.3 DTU

Antarctic IceSheets_CCI+ Round Robin: Ice Velocity on Ice Shelves (IVonIS) Feedback Form	
<u>Participant Information</u>	
Name	Anders Kusk
Affiliation	DTU Space
Address	Ørsteds Plads 348, DK-2800 Lyngby





Email	ak@space.dtu.dk	
<u>Software Specifications</u>	Specify which software(s) were used for data processing. If available, list papers, manuals etc containing the software specifications and documentation.	
	IPP inhouse processor, TMD Tide model driver v2.05 for MATLAB, GDAL 2.2.3, Python 2.7.15	
<u>Processing Specifications</u>	Please provide the following information - alternatively, you may cite a publication where this information is provided.	
Co-registration	Master / Slave Coregistration applied	[Y/N] N
	Brief discription of the co-registration procedure (e.g. how was orbital data used and which refinement algorithm was applied: geometric, data matching, etc)	Precise orbits and DEM only
Pre-Processing procedures:	Brief description of pre-processing routines (e.g. global co-registration procedures, resampling strategies, image enhancements, multi-looking, etc.)	None
Offset estimation	Method applied (e.g. CrossCorrel, Least Squares, etc)	Incoherent cross-correlation
	Matching window size	256x64 (range x azimuth)
	Search window size (if different)	same
	Search window posting	40 x 10 (range x azimuth)
	Oversampling factor (if applicable)	2
	Matching quality measure	CC Peak SNR
	Describe the details of your image matching methods (e.g. variable or constant window sizes, correlation routines, etc.)	Constant window size on regular grid
Post-Processing procedures	Detailed description of all post-processing routines (incl. outlier culling, calibration,	Culling on SNR threshold (7) and NCC threshold (0.05), removal of outliers based on local medians in 5x5 neighbourhood (not median filtering). Subsequent removal of small objects (<=3 pixels) and filling of single-pixel holes

 antarctic ice sheet cci	Antarctica_Ice_Sheet_cci+ Algorithm Theoretical Basis Document (ATBD) for AIS CCI+ Phase 1	Reference: ST-UL-ESA-AISCCI+-ATBD-001 Version : 1.0 page Date : 9 March 2020 47/48
---	--	--

	etc.):	using IDW-interpolation.
	Specific filters applied (e.g. box filter, ionosphere filter)	5x5 averaging filter
Tidal & Atmospheric Pressure Correction	Tidal model used (+version, resolution & source)	CATS2008, August 15, 2017, 4 km resolution. From https://www.esr.org/research/polar-tide-models/list-of-polar-tide-models/cats2008/
	Atmospheric model used (+version, resolution & source)	ERA5 hourly surface pressure, 0.25 x 0.25 degree resolution, from https://cds.climate.copernicus.eu/cdsapp#!/dataset/reanalysis-era5-single-levels?tab=form
	Detailed description of tidal correction-processing routines (include information on: Sampling (one point or grid?); Grid spacing of the used models (any oversampling applied?); Method to handle transition to grounded ice, Any specific parameter settings etc.)	Tide model generated on 4 km x 4km grid for the acquisition times and resampled to output geometry (200 x 200 m). All tide components included (M2, S2, N2, K2, K1, O1, P1, Q1, Mf, Mm). Atmosphere on 0.25x0.25 deg grid retrieved from the nearest hour (8:00) and resampled to output geometry. A vertical displacement is calculated from the tide difference at the two acquisition dates + the surface pressure difference scaled by a factor of 1cm/hPa. The vertical displacement is projected on the line-of-sight to correct the range offsets before calculating horizontal velocities. Transition to grounded ice is handled by using the Measures GLL (retrieved from Quantarctica 3 package), adding a transition zone of 2km from the Measures GL to seaward over which the tidal/pressure correction is increased linearly from 0 at the GL to 100% at the 2km line.
Overall Processing Info	Processing Duration (CPU Time)	The tide correction calculations were negligible compared to the offset-tracking (i.e. a few minutes).

4.7 References

Copernicus Climate Change Service (C3S) (2017): ERA5: Fifth generation of ECMWF atmospheric reanalyses of the global climate . Copernicus Climate Change Service Climate Data Store (CDS), 2 March 2020. <https://cds.climate.copernicus.eu/cdsapp#!/home>

Jansen, D., Luckman, A. J., Cook, A., Bevan, S., Kulesa, B., Hubbard, B., and Holland, P. R.: Brief Communication: Newly developing rift in Larsen C Ice Shelf presents significant risk to stability, *The Cryosphere*, 9, 1223–1227, <https://doi.org/10.5194/tc-9-1223-2015>, 2015.

Rott, H., Abdel Jaber, W., Wuite, J., Scheiblauer, S., Floricioiu, D., van Wessem, J. M., Nagler, T., Miranda, N., and van den Broeke, M. R.: Changing pattern of ice flow and mass balance for glaciers discharging into the Larsen A and B embayments, Antarctic Peninsula, 2011 to 2016, *The Cryosphere*, 12, 1273–1291, <https://doi.org/10.5194/tc-12-1273-2018>, 2018.

Howat, I. M., Porter, C., Smith, B. E., Noh, M.-J., and Morin, P.: The Reference Elevation Model of Antarctica, *The Cryosphere*, 13, 665–674, <https://doi.org/10.5194/tc-13-665-2019>, 2019.

Kalnay, E. et al. (1996) 'The NCEP/NCAR 40-year reanalysis project', *Bulletin of the American meteorological Society*, 77(3), pp. 437–472.



Padman, L., H. A. Fricker, R. Coleman, S. Howard, and S. Erofeeva (2002), A new tidal model for the Antarctic ice shelves and seas, *Ann. Glaciol.*, 34, 247-254. (doi:10.3189/172756402781817752)

Padman, L., L. Erofeeva, and H. A. Fricker (2008), Improving Antarctic tide models by assimilation of ICESat laser altimetry over ice shelves, *Geophys. Res. Lett.*, 35, L22504. (doi:10.1029/2008GL035592)

Pail, Roland; Gruber, Thomas; Fecher, Thomas; GOCO Project Team (2016): The Combined Gravity Model GOCO05c. GFZ Data Services. <http://doi.org/10.5880/icgem.2016.003>

Rignot, E., J. Mouginot, and B. Scheuchl. 2016. MEaSURES Antarctic Grounding Line from Differential Satellite Radar Interferometry, Version 2. [Indicate subset used]. Boulder, Colorado USA. NASA National Snow and Ice Data Center Distributed Active Archive Center. doi: <https://doi.org/10.5067/IKBWW4RYHF1Q>.

End of document